Effects of feedstock availability on the negative ion behavior in a C_4F_8 inductively coupled plasma

Reference:

Zhao Shuxia, Gao Fei, Wang Ya-Ping, Wang You-Nian, Bogaerts Annemie.- Effects of feedstock availability on the negative ion behavior in a C_4F_8 inductively coupled plasma

Journal of applied physics / American Institute of Physics - ISSN 1089-7550 - 118:3(2015), p. 1-18

DOI: http://dx.doi.org/doi:10.1063/1.4926867

Effects of feedstock availability on the negative ion behavior in a C_4F_8 inductively coupled plasma

Shu-Xia Zhao[1,2], Fei Gao[1], Ya-Ping Wang[1], You-Nian Wang[1], and Annemie Bogaerts[2]
[1]School of Physics and Optoelectronic Engineering, Dalian University of Technology, Dalian 116024, People's Republic of China
[2]Research group PLASMANT, Dept. Chemistry, University of Antwerp, Universiteitsplein 1, B-2610 Antwerp, Belgium

Abstract

In this paper, the negative ion behavior in a C_4F_8 inductively coupled plasma (ICP) is investigated using a hybrid model. The model predicts a non-monotonic variation of the total negative ion density with power at low pressure (10-30 mTorr), and this trend agrees well with experiments that were carried out in many fluorocarbon (fc) ICP sources, like C_2F_6, CHF_3 and C_4F_8. This behavior is explained by the availability of feedstock C_4F_8 gas as a source of the negative ions, as well as by the presence of low energy electrons due to vibrational excitation at low power. The maximum of the negative ion density shifts to low power values upon decreasing pressure, because of the more pronounced depletion of C_4F_8 molecules, and at high pressure (~50mTorr), the anion density continuously increases with power, which is similar to fc CCP sources. Furthermore, the negative ion composition is identified in this paper. Our work demonstrates that for a clear understanding of the negative ion behavior in radio frequency C_4F_8 plasma sources, one needs to take into account many factors, like the attachment characteristics, the anion composition, the spatial profiles and the reactor configuration.

Finally, a detailed comparison of our simulation results with experiments is conducted.

I. Introduction

Negative ions are important reactive species in fluorocarbon (fc) plasma sources used for Si-based etching processes. They play a crucial role in (i) the plasma chemistry, particulate and dust formation[1-3], (ii) the plasma physics, plasma instability[4], the formation of a double layer[5] and the drift ambipolar bulk field[6] and modified Bohm velocity[7], as well as in (iii) the etching characteristics, by alleviating the charging effect[8]. Due to their vital role in the fields above, much effort is paid to investigating the negative ion behavior in fc plasmas, like developing diagnostic techniques[9-11], characterizing attachment reactions[12-14], identifying the negative ion composition[15-17], and parametric studies of the anion density by varying pressure and power[18-20] .

Some experiments observed a non-monotonic variation of the negative ion density with applied power at low pressure (10mTorr) in fc inductively coupled plasmas (ICPs)[19, 20], like CHF_3, C_2F_6 and C_4F_8. However, the reason for this trend is not clear yet. In the experimental work of Hebner et al[19, 20], it was related to a power dependent change in the density of one or more of the potential anion precursor species. However, the explanation was not proven by direct evidence, since experimental studies of the anion behavior usually

cannot provide many details of the plasma dynamics. In the modeling work of refs. [21, 22], the non-monotonic variation of the anion density with power was also predicted, and was attributed to the competition between the increasing rates of dissociation and dissociative attachment of the feedstock molecules, caused by an increase in the electron temperature upon increasing power[21]. Nevertheless, these modeling studies were not purely aimed at investigating the negative ion properties and hence not all aspects were taken into account.

We believe that the experimentally observed non-monotonic behavior of the negative ion density is correlated with several factors, the parent attachment characteristics, the anion composition and the spatial characteristics in the plasma. Therefore, it needs a more systematic study. To verify the above considerations, we use in this paper the hybrid plasma equipment model (HPEM) to elaborately study the anion behavior in a C_4F_8 ICP source. The specific goals of this work include: (i) exploring the mechanisms that determine the non-monotonic variation of negative ion density with power at low pressure; (ii) studying the pressure dependence of this non-monotonic behavior in a wider pressure range; and (iii) identifying the negative ion composition.

II. Model description

In this section, the HPEM model is described, together with the ICP reactor

configuration and the C_4F_8 chemical reaction set. The model was developed by Kushner and his team[23-25]. It is composed of several modules and can be used to investigate the electron behavior (like non-local[26] and harmonic effects[27]), the chemical characteristics (like the chemical composition[28]) and the surface kinetics (like etching, deposition and implantation[29]). In this work, the three main modules are applied, i.e., the Fluid Kinetics Module (FKM), the Electron Energy Transport Module (EETM), and the Electromagnetic Module (EMM). The flowchart of the hybrid model is given in Fig. 1. The Fluid Kinetics Module includes a set of fluid equations, like mass, momentum and energy conservation equations of different species, together with the Poisson equation. It is used to describe the behavior of the charged and neutrals species, and the electrostatic field. The two-dimensional profile of the electron conductivity, obtained from this module, is introduced into the EMM to calculate the fields. The EETM can be based on solving the Boltzmann equation or on a Monte Carlo approach. We made use of the latter, the so-called Electron Monte Carlo Module (EMCM). It accounts for the non-local dynamic behavior of electrons at low pressure. It tracks a number of test particles that are advanced by the known electromagnetic (EM) and electrostatic fields, as well as their collisions with neutrals, and it finally collects the trajectories of the electrons to calculate the electron energy distribution functions (eedfs). The transport and rate coefficients of electrons and the electron temperature, used in the fluid equations of the FKM, are

calculated by integrating the eedfs that are multiplied by the related electron-impact cross sections, for the reaction rate coefficients, and by the electron kinetic energy, to obtain the electron temperature. The Electromagnetic Module includes the Maxwell's equations that contain the plasma current density by using the Ohm's heating law. As mentioned above, it produces the spatially revolved EM field. The EM field, together with the electrostatic field from the FKM, are transported back into the EMCM for updating the test particle trajectories. The three modules are iterated with each other until a final steady state is reached. The main equations used in these three modules are given in the Appendix.

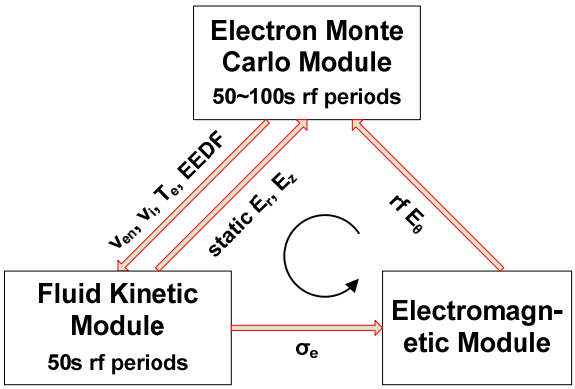

Figure 1. Flowchart of the three main modules in the Hybrid Plasma Equipment Model

The schematic diagram of the ICP reactor considered in this work is given in Fig. 2. The height and radius of the reactor are 18.3cm and 15cm, respectively. Axially, a quartz dielectric window, about 1cm thick and located at about z=14cm, separates the main discharge chamber from the vessel that mounts

the two-turn electromagnetic coil. At the bottom of the chamber, a wafer of 10.5cm in radius is placed. The conventional 13.56MHz power source is supplied to the coil, and for investigating the bulk plasma properties, the wafer is not biased in this work. The gas flows into the chamber through the gas nozzle and it leaves the chamber through the pumping port at the chamber bottom edge. In all cases, the feedstock gas flow rate is fixed at 30sccm. The pressure is varied in the range of 10-50mTorr. Note that the pressure is taken as boundary condition in the fluid equations of the feedstock gas. It is set at the outlet of the chamber. We believe that the bulk of the chamber has a similar pressure as at the outlet, considering that the pressure is low and that a well-stirred approximation can be assumed. The coil power is varied in a wide range, 0.2-4kW, for better understanding the negative ion behavior. We used a constant mesh size of 0.2 cm in the axial and radial direction. This value is much larger than the Debye length, which is in the order of 0.002 cm at the conditions under study, but this is no problem in this type of hybrid model.

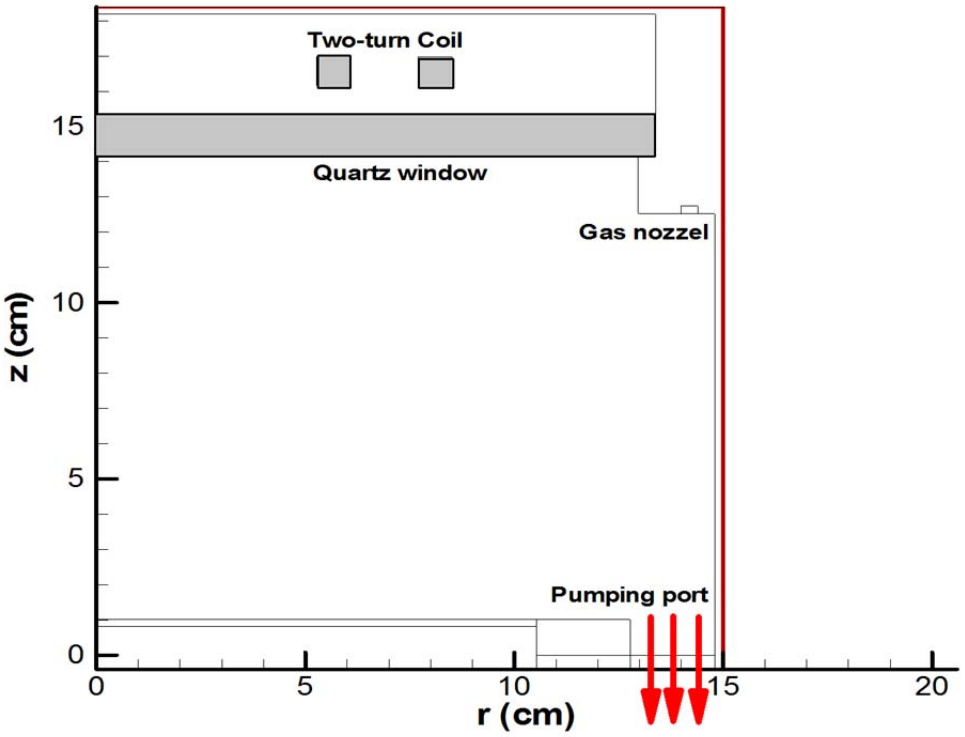

Figure 2. Schematic picture of the ICP reactor assumed in the model.

The reaction set for the C_4F_8 plasma source is mostly based on the work of ref.[28]. It can, in fact, be divided into different sub-sets, which apply to more simple fc plasma sources, like CF_4 and C_2F_6. The reactions of the light CF_a (a=1-4) and C_2F_b (b=3-6) species, including both neutrals and ions, as well as the electron reactions, were presented in our two previous papers[30, 31]. The reactions of the heavy fc species, like C_3F_c and C_4F_d, are listed in ref.[32], where the fragmentation behavior of a C_4F_8 ICP is studied. In the present paper, the reaction subsets of CF_a, C_2F_b and heavy fc species are separately listed in Tables 1, 2 and 3. The references where these reaction data are adopted from can be found in our previously published papers[30-32]. Moreover, in this work, we focus on the various negative ion production processes, i.e., the

parent and dissociative electron attachments with fc species, as well as their loss mechanisms, like autodetachment, collisional stabilization and dissociation of excited parent anions, and neutralization and collisional detachment of F^-. Therefore, these processes are summarized in Table 4 for better reference.

Table 1. Chemical reaction set for the CF_a (a=1-4) species. The rate coefficients or cross sections are all adopted from ref. [30]. The gas temperature (T) is in K.

No.	Reaction	Rate coefficient[a]	Threshold (eV)	Reaction type
1	$e+CF_4 \rightarrow e+CF_4$	c	0	Momentum transfer
2	$e+CF_4 \rightarrow e+CF_4(v2,4)$	c	0.05	Vibrational excitation
3	$e+CF_4 \rightarrow e+CF_4(v1,3)$	c	0.11	Vibrational excitation
4	$e+CF_4 \rightarrow F^-+CF_3$	c	3.0	Dissociative attachment
5	$e+CF_4 \rightarrow CF_3^-+F$	c	4.0	Dissociative attachment
6	$e+CF_4 \rightarrow CF_3^++F+e+e$	c	16.25	Dissociative ionization
7	$e+CF_4 \rightarrow CF_3^++F^++e+e+e$	c	35.0	Dissociative ionization
8	$e+CF_4 \rightarrow CF_2^++F+F+e+e$	c	20.0	Dissociative ionization
9	$e+CF_4 \rightarrow CF^++F+F_2+e+e$	c	25.0	Dissociative ionization
10	$e+CF_4 \rightarrow F^++CF_3+e+e$	c	30.0	Dissociative ionization
11	$e+CF_4 \rightarrow CF_3+F+e$	c	12.0	Dissociation
12	$e+CF_4 \rightarrow CF_2+F+F+e$	c	14.0	Dissociation
13	$e+CF_4 \rightarrow CF+F+F_2+e$	c	18.0	Dissociation
14	$e+CF_3 \rightarrow CF_3+e$	c	0	Momentum transfer
15	$e+CF_3 \rightarrow e+CF_3(v2,4)$	c	0.05	Vibrational excitation
16	$e+CF_3 \rightarrow e+CF_3(v1,3)$	c	0.11	Vibrational excitation
17	$e+CF_3 \rightarrow F^-+CF_2$	c	4.4	Dissociative attachment
18	$e+CF_3 \rightarrow CF_2+F+e$	c	7.7	Dissociation
19	$e+CF_3 \rightarrow CF_3^++e+e$	c	8.9	Ionization
20	$e+CF_3 \rightarrow CF_2^++F+e+e$	c	17.0	Dissociative ionization
21	$e+CF_3 \rightarrow CF^++F+F+e+e$	c	20.0	Dissociative ionization
22	$e+CF_3 \rightarrow F^++CF_2+e+e$	c	20.0	Dissociative ionization
23	$e+CF_3^+ \rightarrow CF_2+F$	c	0	Dissociative

				recombination
24	$e+CF_2 \rightarrow CF_2+e$	c	0	Momentum transfer
25	$e+CF_2 \rightarrow e+CF_2(v2,4)$	c	0.05	Vibrational excitation
26	$e+CF_2 \rightarrow e+CF_2(v1,3)$	c	0.11	Vibrational excitation
27	$e+CF_2 \rightarrow F^-+CF$	c	4.4	Dissociative attachment
28	$e+CF_2 \rightarrow CF+F+e$	c	8.7	Dissociation
29	$e+CF_2 \rightarrow CF_2^+ +e+e$	c	11.0	Ionization
30	$e+CF_2 \rightarrow CF^+ +F+e+e$	c	14.0	Dissociative ionization
31	$e+CF_2 \rightarrow F^+ +CF+e+e$	c	30.0	Dissociative ionization
32	$e+CF_2^+ \rightarrow CF+F$	c	0	Dissociative recombination
33	$e+CF \rightarrow CF+e$	c	0	Momentum transfer
34	$e+CF \rightarrow e+CF(v2)$	c	0.14	Vibrational excitation
35	$e+CF \rightarrow C+F+e$	c	5.6	Dissociation
36	$e+CF \rightarrow CF^+ +e+e$	c	10.38	Ionization
37	$e+F_2 \rightarrow F_2+e$	c	0	Momentum transfer
38	$e+F_2 \rightarrow F_2(v)+e$	c	0.11	Vibrational excitation
39	$e+F_2 \rightarrow F^-+F$	c	0	Dissociative attachment
40	$e+F_2 \rightarrow e+F_2(*) \rightarrow F+F+e$	c	3.16	Excitation & dissociation
41	$e+F_2 \rightarrow e+F_2(*) \rightarrow F+F+e$	c	4.34	Excitation & dissociation
42	$e+F_2 \rightarrow F_2(*)+e$	c	11.57	Excitation[b]
43	$e+F_2 \rightarrow F_2(*)+e$	c	13.08	Excitation[b]
44	$e+F_2 \rightarrow F_2^+ +e+e$	c	15.69	Ionization
45	$e+F_2^+ \rightarrow F+F$	c	0	Dissociative recombination
46	$e+F \rightarrow F+e$	c	0	Momentum transfer
47	$e+F \rightarrow F^* +e$	c	12.70	Excitation
48	$e+F \rightarrow F^+ +e+e$	c	17.42	Ionization
49	$e+F^* \rightarrow F+e$	c	-12.7	Superelastic collision
50	$e+F^* \rightarrow F^+ +e+e$	c	0	Multistep ionization
51	$e+F^+ \rightarrow F$	c	0	Recombination
52	$F^-+CF_3^+ \rightarrow CF_2+F_2$	8.7×10^{-8}	0	Dissociative recombination
53	$F^-+CF_3^+ \rightarrow CF_2+F+F$	$3.0\times10^{-7}\times(T/298.)^{-0.5}$	0	Dissociative recombination
54	$F^-+CF_3^+ \rightarrow CF_3+F$	3.0×10^{-7}	0	Recombination
55	$F^-+CF_2^+ \rightarrow CF+F_2$	9.1×10^{-8}	0	Dissociative recombination
56	$F^-+CF_2^+ \rightarrow CF_2+F$	5.0×10^{-7}	0	Recombination
57	$F^-+CF^+ \rightarrow CF+F$	9.8×10^{-8}	0	Recombination
58	$F^-+CF^+ \rightarrow C+F+F$	7.0×10^{-7}	0	Dissociative

		$\times(T/298.)^{-0.5}$		recombination
59	$F^-+F_2^+\rightarrow F+F_2$	9.4×10^{-8}	0	Recombination
60	$F^-+F^+\rightarrow F+F$	7.1×10^{-7}	0	Recombination
61	$CF_3^-+CF_3^+\rightarrow CF_3+CF_3$	3.0×10^{-7}	0	Recombination
62	$CF_3^-+CF_2^+\rightarrow CF_3+CF_2$	5.0×10^{-7}	0	Recombination
63	$CF_3^-+CF^+\rightarrow CF_3+CF$	7.0×10^{-7}	0	Recombination
64	$CF_3^-+F^+\rightarrow CF_3+F$	7.0×10^{-7}	0	Recombination
65	$CF_3^-+F_2^+\rightarrow CF_3+F_2$	5.0×10^{-7}	0	Recombination
66	$F^-+CF_3\rightarrow CF_4+e$	4.0×10^{-10}	0	Detachment
67	$F^-+CF_2\rightarrow CF_3+e$	3.0×10^{-10}	0	Detachment
68	$F^-+CF\rightarrow CF_2+e$	2.0×10^{-10}	0	Detachment
69	$F^-+C\rightarrow CF+e$	1.0×10^{-10}	0	Detachment
70	$F^-+F\rightarrow F_2+e$	1.0×10^{-10}	0	Detachment
71	$F+CF_3\rightarrow CF_4$	2.0×10^{-11}	0	Recombination
72	$F+CF_2\rightarrow CF_3$	1.8×10^{-11}	0	Recombination
73	$F+CF\rightarrow CF_2$	9.96×10^{-11}	0	Recombination
74	$F_2+CF_3\rightarrow CF_4+F$	1.88×10^{-14}	0	Recombination
75	$F_2+CF_2\rightarrow CF_3+F$	8.3×10^{-14}	0	Recombination
76	$CF_3^++CF_3\rightarrow CF_3^++CF_3$	1.0×10^{-9}	0	Charge exchange
77	$CF_2^++CF_4\rightarrow CF_3^++CF_3$	4.0×10^{-10}	0	Charge and atom exchange
78	$CF_2^++CF_3\rightarrow CF_3^++CF_2$	1.48×10^{-9}	0	Charge exchange
79	$CF_2^++CF_2\rightarrow CF_2^++CF_2$	1.0×10^{-9}	0	Charge exchange
80	$CF_2^++CF\rightarrow CF_3^++C$	2.06×10^{-9}	0	Charge and atom exchange
81	$CF_2^++C\rightarrow CF^++CF$	1.04×10^{-9}	0	Charge and atom exchange
82	$CF^++CF_4\rightarrow CF_3^++CF_2$	1.8×10^{-10}	0	Charge and atom exchange
83	$CF^++CF_3\rightarrow CF_3^++CF$	1.71×10^{-9}	0	Charge exchange
84	$CF^++CF\rightarrow CF^++CF$	2.0×10^{-10}	0	Charge exchange
85	$F^++CF_4\rightarrow CF_3^++F_2$	1.0×10^{-9}	0	Charge and atom exchange
86	$F^++CF_3\rightarrow CF_2^++F_2$	1.09×10^{-9}	0	Charge and atom exchange
87	$F^++CF_2\rightarrow CF^++F_2$	2.28×10^{-9}	0	Charge and atom exchange

88	$F^+ + F_2 \rightarrow F_2^+ + F$	7.94×10^{-10}	0	Charge exchange
89	$F^+ + F \rightarrow F^+ + F$	1.0×10^{-9}	0	Charge exchange
90	$F_2^+ + CF_4 \rightarrow CF_3^+ + F + F_2$	1.0×10^{-10}	0	Charge and atom exchange
91	$F_2^+ + CF_3 \rightarrow CF_3^+ + F + F$	1.6×10^{-9}	0	Charge and atom exchange
92	$F_2^+ + CF_2 \rightarrow CF_2^+ + F_2$	1.0×10^{-9}	0	Charge exchange
93	$F_2^+ + CF_2 \rightarrow CF_3^+ + F$	1.79×10^{-9}	0	Charge and atom exchange
94	$F_2^+ + CF \rightarrow CF_2^+ + F$	2.18×10^{-9}	0	Charge and atom exchange
95	$F_2^+ + C \rightarrow CF^+ + F$	1.04×10^{-9}	0	Charge and atom exchange
96	$F_2^+ + F_2 \rightarrow F_2^+ + F_2$	1.0×10^{-9}	0	Charge exchange
97	$CF_3^- + F \rightarrow CF_3 + F^-$	5.0×10^{-8}	0	Charge exchange

[a]The unit of the rate coefficient is cm^3s^{-1}. The letter c represents that the coefficient is calculated from the electron Monte Carlo module based on the corresponding electron impact cross sections.

[b]The excited F2 species found in the reactions (42) and (43) are not considered as separate species in the model, but the reactions are included because they affect the electron energy.

Table 2. Chemical reaction set for C_2F_b (b=3-6) species. The rate coefficients or cross sections are all adopted from ref. [31] The electron temperature (T_e) is in eV.

No.	**Reaction**	**Rate coefficient[a]**	**Threshold (eV)**	**Reaction type**
1	$e + C_2F_6 \rightarrow e + C_2F_6$	c	0	Momentum transfer
2	$e + C_2F_6 \rightarrow e + C_2F_6(v1)$	c	0.089	Vibrational excitation
3	$e + C_2F_6 \rightarrow e + C_2F_6(v2)$	c	0.1387	Vibrational excitation
4	$e + C_2F_6 \rightarrow e + C_2F_6(v3)$	c	0.155	Vibrational excitation
5	$e + C_2F_6 \rightarrow e + C_2F_6(*)$	c	7.2	Electronic excitation[b]
6	$e + C_2F_6 \rightarrow e + CF_3 + CF_3$	c	12.3	Dissociation
7	$e + C_2F_6 \rightarrow e + e + CF_3^+ + CF_3$	c	14.2	Dissociative ionization
8	$e + C_2F_6 \rightarrow CF_3 + CF_3^-$	c	2.494	Dissociative attachment
9	$e + C_2F_6 \rightarrow C_2F_5 + F^-$	c	2.494	Dissociative attachment
10	$e + C_2F_5 \rightarrow C_2F_5 + e$	c	0	Momentum transfer
11	$e + C_2F_5 \rightarrow C_2F_5(v1) + e$	c	0.089	Vibrational excitation
12	$e + C_2F_5 \rightarrow C_2F_5(v2) + e$	c	0.1387	Vibrational excitation
13	$e + C_2F_5 \rightarrow C_2F_5(v3) + e$	c	0.155	Vibrational excitation
14	$e + C_2F_5 \rightarrow e + C_2F_5(*)$	c	7.2	Electronic excitation[b]

15	$e+C_2F_5 \rightarrow e+CF_3+CF_2$	c	12.3	Dissociation
16	$e+C_2F_5 \rightarrow e+e+CF_3^+ + CF_2$	c	14.5	Dissociative ionization
17	$e+C_2F_5 \rightarrow e+e+C_2F_5^+$	c	12.5	Ionization
18	$e+C_2F_5 \rightarrow CF_2+CF_3^-$	c	2.494	Dissociative attachment
19	$e+C_2F_4 \rightarrow e+C_2F_4$	c	0	Momentum transfer
20	$e+C_2F_4 \rightarrow e+C_2F_4(v1)$	c	0.16	Vibrational excitation
21	$e+C_2F_4 \rightarrow e+C_2F_4(v2)$	c	0.23	Vibrational excitation
22	$e+C_2F_4 \rightarrow CF_2+CF_2$	c	5.0	Dissociation
23	$e+C_2F_4 \rightarrow e+e+C_2F_4^+$	c	9.89	Ionization
24	$e+C_2F_4 \rightarrow e+e+C_2F_3^+ + F$	c	15.85	Dissociative ionization
25	$e+C_2F_4 \rightarrow e+e+CF^+ + CF_3$	c	17.68	Dissociative ionization
26	$e+C_2F_3 \rightarrow e+CF_2+CF$	$1.0\times10^{-8} \times T_e^{0.906}\times\exp(-5.0/T_e)$	2.0	Dissociation[c]
27	$e+C_2F_5^+ \rightarrow CF_2+CF_3$	$8.0\times10^{-8} \times T_e^{-0.5}$	4.0	Dissociative recombination[c]
28	$e+C_2F_4^+ \rightarrow CF_2+CF_2$	$8.0\times10^{-8} \times T_e^{-0.5}$	4.0	Dissociative recombination[c]
29	$e+C_2F_3^+ \rightarrow CF_2+CF$	$8.0\times10^{-8} \times T_e^{-0.5}$	5.0	Dissociative recombination[c]
30	$F^-+C_2F_5^+ \rightarrow F+C_2F_5$	8.0×10^{-8}	0	Recombination
31	$F^-+C_2F_4^+ \rightarrow CF+CF_2+F_2$	8.2×10^{-8}	0	Dissociative recombination
32	$F^-+C_2F_3^+ \rightarrow F+C_2F_3$	8.0×10^{-8}	0	Recombination
33	$CF_3^-+C_2F_5^+ \rightarrow CF_3+C_2F_5$	1.0×10^{-7}	0	Recombination
34	$CF_3^-+C_2F_4^+ \rightarrow CF_3+C_2F_4$	1.0×10^{-7}	0	Recombination
35	$CF_3^-+C_2F_3^+ \rightarrow CF_3+C_2F_3$	1.0×10^{-7}	0	Recombination
36	$CF_3+CF_3^- \rightarrow C_2F_6+e$	1.0×10^{-10}	0	Electron detachment
37	$C+C_2F_4 \rightarrow C_2F_3+CF$	1.91×10^{-10}	0	Atom exchange
38	$F+C_2F_4 \rightarrow CF_3+CF_2$	4.8×10^{-11}	0	Atom exchange
39	$F+C_2F_5 \rightarrow CF_3+CF_3$	1.0×10^{-11}	0	Atom exchange
40	$F+C_2F_3 \rightarrow C_2F_4$	1.0×10^{-12}	0	Atom exchange
41	$F_2+C_2F_4 \rightarrow C_2F_5+F$	3.5×10^{-16}	0	Atom exchange
42	$CF_2+CF_3 \rightarrow C_2F_5$	1.0×10^{-12}	0	Atom exchange
43	$CF_3+CF_3+M \rightarrow M+C_2F_6$	3.94×10^{-29}	0	Atom exchange[d]
44	$CF_3+CF_3 \rightarrow C_2F_6$	8.3×10^{-12}	0	Atom exchange

45	$CF_2+CF_2\rightarrow C_2F_4$	7.21×10^{-14}	0	Atom exchange
46	$CF_3^++C_2F_6\rightarrow C_2F_5^++CF_4$	2.5×10^{-12}	0	Charge exchange
47	$CF_2^++C_2F_4\rightarrow C_2F_4^++CF_2$	1.0×10^{-9}	0	Charge exchange
48	$CF_2^++C_2F_6\rightarrow C_2F_5^++CF_3$	3.5×10^{-11}	0	Charge exchange
49	$CF^++C_2F_4\rightarrow CF_3^++CF+CF$	2.6×10^{-10}	0	Charge exchange
50	$CF^++C_2F_6\rightarrow CF_3^++C_2F_4$	2.0×10^{-10}	0	Charge exchange
51	$F^++C_2F_6\rightarrow C_2F_5^++F_2$	1.0×10^{-9}	0	Charge exchange
52	$F^++C_2F_5\rightarrow C_2F_4^++F_2$	1.0×10^{-9}	0	Charge exchange
53	$F^++C_2F_4\rightarrow C_2F_4^++F$	1.0×10^{-9}	0	Charge exchange
54	$F_2^++C_2F_5\rightarrow C_2F_5^++F_2$	1.0×10^{-10}	0	Charge exchange
55	$F_2^++C_2F_4\rightarrow C_2F_4^++F_2$	1.0×10^{-10}	0	Charge exchange
56	$C_2F_4^++C_2F_4\rightarrow C_2F_4+C_2F_4^+$	4.0×10^{-9}	0	Charge exchange[e]
57	$C_2F_5^++C_2F_5\rightarrow C_2F_5+C_2F_5^+$	4.0×10^{-9}	0	Charge exchange[e]

[a]The unit of the rate coefficient is cm^3s^{-1}. The letter c represents that the coefficient is calculated from the electron Monte Carlo module based on the corresponding electron impact cross sections.

[b]The excited C_2F_6 and C_2F_5 species found in reactions (5) and (14), respectively, are not considered as separate species in the model, but the reactions are included because they affect the electron energy.

[c]In the expression of the rate coefficients, T_e represents the electron temperature, with units of eV.

[d]This is a three-body reaction. M stands for the third body and represents the sum of all neutrals considered in the model. The rate coefficient of this reaction is in units of $cm^6\ s^{-1}$.

[e]The charge exchange reactions (56) and (57) do not change the density of the reacting species, but only their momentum and energy by means of the momentum and energy balance equations of ions and neutrals.

Table 3. Chemical reactions for the C_3F_c and C_4F_d species considered in the model. The rate coefficients or cross sections are all adopted from ref. [32]. The electron temperature (T_e) is in eV.

No.	**Reaction**	**Rate coefficient[a]**	**Threshold (eV)**	**Reaction type**
1	$e+C_3F_5\rightarrow C_2F_3+CF_2+e$	$1.8\times10^{-8}\times T_e^{0.52}\times \exp\left(-\frac{12.3}{T_e}\right)$	5.0	Dissociation
2	$e+C_3F_5\rightarrow C_2F_4+CF+e$	$1.8\times10^{-8}\times$	5.0	Dissociation

		$T_e^{0.52} \times \exp\left(-\frac{12.3}{T_e}\right)$		
3	$e+C_3F_5^+ \rightarrow C_2F_3+CF_2$	$8.0 \times 10^{-8} \times T_e^{-0.5}$	0.0	Dissociative recombination
4	$e+C_3F_6 \rightarrow C_3F_6^+ +e+e$	$1.4 \times 10^{-8} \times T_e^{0.68} \times \exp\left(-\frac{10.6}{T_e}\right)$	9.89	Parent ionization
5	$e+C_3F_6 \rightarrow C_2F_3+CF_3+e$	$1.8 \times 10^{-8} \times T_e^{0.52} \times \exp\left(-\frac{12.3}{T_e}\right)$	5.0	Dissociation
6	$e+C_3F_6 \rightarrow C_2F_4+CF_2+e$	$1.8 \times 10^{-8} \times T_e^{0.52} \times \exp\left(-\frac{12.3}{T_e}\right)$	5.0	Dissociation
7	$e+C_3F_6^+ \rightarrow C_2F_4+CF_2$	$8.0 \times 10^{-8} \times T_e^{-0.5}$	0.0	Dissociative recombination
8	$e+C_3F_7 \rightarrow C_2F_4+CF_3+e$	$1.8 \times 10^{-8} \times T_e^{0.52} \times \exp\left(-\frac{12.3}{T_e}\right)$	5.0	Dissociation
9	$e+C_3F_7^+ \rightarrow C_2F_4+CF_3$	$8.0 \times 10^{-8} \times T_e^{-0.5}$	0.0	Dissociative recombination
10	$e+C_4F_7 \rightarrow C_2F_4+C_2F_3+e$	$5.7 \times 10^{-8} \times T_e^{0.28} \times \exp\left(-\frac{8.0}{T_e}\right)$	12.3	Dissociation
11	$e+C_4F_7 \rightarrow C_4F_7^+ +e+e$	$1.4 \times 10^{-8} \times T_e^{0.68} \times \exp\left(-\frac{10.6}{T_e}\right)$	14.2	Parent ionization
12[b]	$e+C_4F_7^+ \rightarrow C_2F_4+C_2F_3$	$8.0 \times 10^{-8} \times T_e^{-0.5}$	0.0	Dissociative recombination
13	$e+C_4F_8 \rightarrow C_4F_8+e$	c	0.0	Momentum transfer
14	$e+C_4F_8 \rightarrow C_4F_8(v1)+e$	c	0.12	Vibrational excitation
15	$e+C_4F_8 \rightarrow C_2F_4+C_2F_4+e$	c	8.0	Dissociation
16	$e+C_4F_8 \rightarrow C_4F_8^{-*}$	c	0.0	Excited parent attachment
17	$e+C_4F_8 \rightarrow F^- +C_4F_7$	c	3.0	Dissociative attachment

18	$e+C_4F_8 \rightarrow C_3F_5^+ + CF_3 + e + e$	c	11.5	Dissociative ionization
19	$e+C_4F_8 \rightarrow C_2F_4^+ + C_2F_4 + e + e$	c	12.3	Dissociative ionization
20	$e+C_4F_8 \rightarrow F^+ + C_4F_7 + e + e$	c	12.9	Dissociative ionization
21	$e+C_4F_8 \rightarrow CF_3^+ + C_3F_5 + e + e$	c	12.7	Dissociative ionization
22	$e+C_4F_8 \rightarrow CF_2^+ + C_3F_6 + e + e$	c	13.4	Dissociative ionization
23	$e+C_4F_8 \rightarrow CF^+ + C_3F_7 + e + e$	c	14.1	Dissociative ionization
24	$e+C_4F_8 \rightarrow C_3F_6 + CF_2 + e$	c	10.0	Dissociation
25	$F^- + C_3F_5^+ \rightarrow C_2F_4 + CF_2$	8.0×10^{-8}	0	Recombination
26	$F^- + C_3F_6^+ \rightarrow C_2F_4 + CF_3$	8.0×10^{-8}	0	Recombination
27	$F^- + C_3F_7^+ \rightarrow C_2F_6 + CF_2$	8.0×10^{-8}	0	Recombination
28	$F^- + C_4F_7^+ \rightarrow C_2F_5 + C_2F_3$	8.0×10^{-8}	0	Recombination
29	$CF_3^- + C_3F_5^+ \rightarrow CF_3 + C_3F_5$	1.0×10^{-7}	0	Recombination
30	$CF_3^- + C_3F_6^+ \rightarrow CF_3 + C_3F_6$	1.0×10^{-7}	0	Recombination
31	$CF_3^- + C_3F_7^+ \rightarrow CF_3 + C_3F_7$	1.0×10^{-7}	0	Recombination
32	$CF_3^- + C_4F_7^+ \rightarrow CF_3 + C_4F_7$	1.0×10^{-7}	0	Recombination
33	$C_4F_8^- + F^+ \rightarrow C_4F_8 + F$	2.0×10^{-7}	0	Recombination
34	$C_4F_8^- + F_2^+ \rightarrow C_4F_8 + F_2$	1.5×10^{-7}	0	Recombination
35	$C_4F_8^- + C^+ \rightarrow C_4F_8 + C$	3.0×10^{-7}	0	Recombination
36	$C_4F_8^- + CF^+ \rightarrow C_4F_8 + CF$	1.5×10^{-7}	0	Recombination
37	$C_4F_8^- + CF_2^+ \rightarrow C_4F_8 + CF_2$	1.0×10^{-7}	0	Recombination
38	$C_4F_8^- + CF_3^+ \rightarrow C_4F_8 + CF_3$	1.0×10^{-7}	0	Recombination
39	$C_4F_8^- + C_2F_3^+ \rightarrow C_4F_8 + C_2F_3$	9.0×10^{-8}	0	Recombination
40	$C_4F_8^- + C_2F_4^+ \rightarrow C_4F_8 + C_2F_4$	9.0×10^{-8}	0	Recombination
41	$C_4F_8^- + C_2F_5^+ \rightarrow C_4F_8 + C_2F_5$	9.0×10^{-8}	0	Recombination
42	$C_4F_8^- + C_3F_5^+ \rightarrow C_4F_8 + C_3F_5$	9.0×10^{-8}	0	Recombination
43	$C_4F_8^- + C_3F_6^+ \rightarrow C_4F_8 + C_3F_6$	9.0×10^{-8}	0	Recombination
44	$C_4F_8^- + C_3F_7^+ \rightarrow C_4F_8 + C_3F_7$	9.0×10^{-8}	0	Recombination
45	$C_4F_8^- + C_4F_7^+ \rightarrow C_4F_8 + C_4F_7$	9.0×10^{-8}	0	Recombination
46	$C_4F_8^{-*} + F^+ \rightarrow C_4F_8 + F$	2.0×10^{-7}	0	De-excitation & Recombination
47	$C_4F_8^{-*} + F_2^+ \rightarrow C_4F_8 + F_2$	1.5×10^{-7}	0	De-excitation & Recombination
48	$C_4F_8^{-*} + C^+ \rightarrow C_4F_8 + C$	3.0×10^{-7}	0	De-excitation & Recombination
49	$C_4F_8^{-*} + CF^+ \rightarrow C_4F_8 + CF$	1.5×10^{-7}	0	De-excitation & Recombination
50	$C_4F_8^{-*} + CF_2^+ \rightarrow C_4F_8 + CF_2$	1.0×10^{-7}	0	De-excitation &

				Recombination
51	$C_4F_8^{-*}+CF_3^+ \rightarrow C_4F_8+CF_3$	1.0×10^{-7}	0	De-excitation & Recombination
52	$C_4F_8^{-*}+C_2F_3^+ \rightarrow C_4F_8+C_2F_3$	9.0×10^{-8}	0	De-excitation & Recombination
53	$C_4F_8^{-*}+C_2F_4^+ \rightarrow C_4F_8+C_2F_4$	9.0×10^{-8}	0	De-excitation & Recombination
54	$C_4F_8^{-*}+C_2F_5^+ \rightarrow C_4F_8+C_2F_5$	9.0×10^{-8}	0	De-excitation & Recombination
55	$C_4F_8^{-*}+C_3F_5^+ \rightarrow C_4F_8+C_3F_5$	9.0×10^{-8}	0	De-excitation & Recombination
56	$C_4F_8^{-*}+C_3F_6^+ \rightarrow C_4F_8+C_3F_6$	9.0×10^{-8}	0	De-excitation & Recombination
57	$C_4F_8^{-*}+C_3F_7^+ \rightarrow C_4F_8+C_3F_7$	9.0×10^{-8}	0	De-excitation & Recombination
58	$C_4F_8^{-*}+C_4F_7^+ \rightarrow C_4F_8+C_4F_7$	9.0×10^{-8}	0	De-excitation & Recombination
59	$F+C_4F_7 \rightarrow C_2F_4+C_2F_4$	1.0×10^{-11}	0	Atom exchange
60	$F+C_3F_6 \rightarrow C_3F_7$	1.0×10^{-12}	0	Recombination
61	$F_2+C_3F_6 \rightarrow C_3F_7+F$	3.5×10^{-16}	0	Atom exchange
62	$CF_3^++C_3F_5 \rightarrow C_3F_5^++CF_3$	7.04×10^{-10}	0	Charge exchange
63	$CF_3^++C_3F_7 \rightarrow C_3F_7^++CF_3$	7.04×10^{-10}	0	Charge exchange
64	$C_4F_8^-+F \rightarrow C_4F_8+F^-$	1.0×10^{-9}	0	Charge exchange
65	$C_4F_8^{-*}+M \rightarrow C_4F_8^-+M$	1.0×10^{-10}	0	De-excitation
66	$C_4F_8^{-*} \rightarrow C_4F_8+e$	1.0×10^{5}	0	Autodetachment
67	$C_3F_5^++C_3F_5 \rightarrow C_3F_5+C_3F_5^+$	3.0×10^{-9}	0	Charge exchange
68	$C_3F_7^++C_3F_7 \rightarrow C_3F_7+C_3F_7^+$	3.0×10^{-9}	0	Charge exchange
69	$C_3F_7^++C_2F_4 \rightarrow C_4F_8+CF_3^+$	2.0×10^{-11}	0	Charge & atom exchange

[a]The unit of the rate coefficient is cm^3s^{-1} for the two-body reactions. The letter c means that the rate coefficient is calculated from the electron energy transport module based on the corresponding electron impact cross sections.

[b]The rate coefficients of the first 1-12 reactions are obtained from by integrating a Maxwellian EEDF, whereas in reality the EEDF might deviate from a Maxwellian distribution. However, it is believed that this approximation will not affect the final results too much since these heavy species are not predominant in the discharges.

In the surface reaction set, all ions and excited neutrals are recycled back into the plasma as ground-state neutrals, after neutralization and de-excitation, respectively. The F atoms and light fc neutrals are assumed to stick to the surface with specific probabilities, as explained in detail in ref. [30]. The heavy

fc neutrals are all reflected from the surface into the plasma. We believe that this assumption will not strongly influence the main characteristics of this fc plasma source, since many experiments already revealed that light fc neutrals indeed dominate over heavy polymeric species in a C_4F_8 plasma[33-36]. The F and CF_3 neutrals will recombine with themselves after sticking on the surface, and return into the plasma as F_2 and C_2F_6 molecules, respectively. More details about the surface reaction set can be found in refs. [30-32].

Table 4. Reactions of negative ion production and loss channels in a C_4F_8 plasma source, included in our model. The rate coefficients or cross sections are all adopted from refs. [30-32]. The gas temperature (T) is in K.

No.	Reaction	Rate coefficient[a]	Threshold (eV)	Reaction type
1	$e+CF_4 \rightarrow F^-+CF_3$	c	3.0	Dissociative attachment
2	$e+CF_4 \rightarrow CF_3^-+F$	c	4.0	Dissociative attachment
3	$e+CF_3 \rightarrow F^-+CF_2$	c	4.4	Dissociative attachment
4	$e+CF_2 \rightarrow F^-+CF$	c	4.4	Dissociative attachment
5	$e+C_2F_6 \rightarrow CF_3+CF_3^-$	c	2.494	Dissociative attachment
6	$e+C_2F_6 \rightarrow C_2F_5+F^-$	c	2.494	Dissociative attachment
7	$e+C_2F_5 \rightarrow CF_2+CF_3^-$	c	2.494	Dissociative attachment
8	$e+C_4F_8 \rightarrow C_4F_8^{-*}$	c	0.0	Excited parent attachment[b]
9	$e+C_4F_8 \rightarrow F^-+C_4F_7$	c	3.0	Dissociative attachment
10	$F^-+C_3F_5^+ \rightarrow C_2F_4+CF_2$	8.0×10^{-8}	0	Recombination
11	$F^-+C_3F_6^+ \rightarrow C_2F_4+CF_3$	8.0×10^{-8}	0	Recombination
12	$F^-+C_3F_7^+ \rightarrow C_2F_6+CF_2$	8.0×10^{-8}	0	Recombination
13	$F^-+C_4F_7^+ \rightarrow C_2F_5+C_2F_3$	8.0×10^{-8}	0	Recombination
14	$CF_3^-+C_3F_5^+ \rightarrow CF_3+C_3F_5$	1.0×10^{-7}	0	Recombination
15	$CF_3^-+C_3F_6^+ \rightarrow CF_3+C_3F_6$	1.0×10^{-7}	0	Recombination
16	$CF_3^-+C_3F_7^+ \rightarrow CF_3+C_3F_7$	1.0×10^{-7}	0	Recombination
17	$CF_3^-+C_4F_7^+ \rightarrow CF_3+C_4F_7$	1.0×10^{-7}	0	Recombination
18	$C_4F_8^-+F^+ \rightarrow C_4F_8+F$	2.0×10^{-7}	0	Recombination
19	$C_4F_8^-+F_2^+ \rightarrow C_4F_8+F_2$	1.5×10^{-7}	0	Recombination
20	$C_4F_8^-+C^+ \rightarrow C_4F_8+C$	3.0×10^{-7}	0	Recombination

21	$C_4F_8^- + CF^+ \rightarrow C_4F_8 + CF$	1.5×10^{-7}	0	Recombination
21	$C_4F_8^- + CF_2^+ \rightarrow C_4F_8 + CF_2$	1.0×10^{-7}	0	Recombination
22	$C_4F_8^- + CF_3^+ \rightarrow C_4F_8 + CF_3$	1.0×10^{-7}	0	Recombination
23	$C_4F_8^- + C_2F_3^+ \rightarrow C_4F_8 + C_2F_3$	9.0×10^{-8}	0	Recombination
24	$C_4F_8^- + C_2F_4^+ \rightarrow C_4F_8 + C_2F_4$	9.0×10^{-8}	0	Recombination
25	$C_4F_8^- + C_2F_5^+ \rightarrow C_4F_8 + C_2F_5$	9.0×10^{-8}	0	Recombination
26	$C_4F_8^- + C_3F_5^+ \rightarrow C_4F_8 + C_3F_5$	9.0×10^{-8}	0	Recombination
27	$C_4F_8^- + C_3F_6^+ \rightarrow C_4F_8 + C_3F_6$	9.0×10^{-8}	0	Recombination
28	$C_4F_8^- + C_3F_7^+ \rightarrow C_4F_8 + C_3F_7$	9.0×10^{-8}	0	Recombination
29	$C_4F_8^- + C_4F_7^+ \rightarrow C_4F_8 + C_4F_7$	9.0×10^{-8}	0	Recombination
30	$C_4F_8^{-*} + F^+ \rightarrow C_4F_8 + F$	2.0×10^{-7}	0	De-excitation & Recombination
31	$C_4F_8^{-*} + F_2^+ \rightarrow C_4F_8 + F_2$	1.5×10^{-7}	0	De-excitation & Recombination
32	$C_4F_8^{-*} + C^+ \rightarrow C_4F_8 + C$	3.0×10^{-7}	0	De-excitation & Recombination
33	$C_4F_8^{-*} + CF^+ \rightarrow C_4F_8 + CF$	1.5×10^{-7}	0	De-excitation & Recombination
34	$C_4F_8^{-*} + CF_2^+ \rightarrow C_4F_8 + CF_2$	1.0×10^{-7}	0	De-excitation & Recombination
35	$C_4F_8^{-*} + CF_3^+ \rightarrow C_4F_8 + CF_3$	1.0×10^{-7}	0	De-excitation & Recombination
36	$C_4F_8^{-*} + C_2F_3^+ \rightarrow C_4F_8 + C_2F_3$	9.0×10^{-8}	0	De-excitation & Recombination
37	$C_4F_8^{-*} + C_2F_4^+ \rightarrow C_4F_8 + C_2F_4$	9.0×10^{-8}	0	De-excitation & Recombination
38	$C_4F_8^{-*} + C_2F_5^+ \rightarrow C_4F_8 + C_2F_5$	9.0×10^{-8}	0	De-excitation & Recombination
39	$C_4F_8^{-*} + C_3F_5^+ \rightarrow C_4F_8 + C_3F_5$	9.0×10^{-8}	0	De-excitation & Recombination
40	$C_4F_8^{-*} + C_3F_6^+ \rightarrow C_4F_8 + C_3F_6$	9.0×10^{-8}	0	De-excitation & Recombination
41	$C_4F_8^{-*} + C_3F_7^+ \rightarrow C_4F_8 + C_3F_7$	9.0×10^{-8}	0	De-excitation & Recombination
42	$C_4F_8^{-*} + C_4F_7^+ \rightarrow C_4F_8 + C_4F_7$	9.0×10^{-8}	0	De-excitation & Recombination
43	$C_4F_8^{-*} + M \rightarrow C_4F_8^- + M$	1.0×10^{-10}	0	De-excitation[b]
44	$C_4F_8^{-*} \rightarrow C_4F_8 + e$	1.0×10^{5}	0	Autodetachment[c]
45	$F^- + CF_3^+ \rightarrow CF_2 + F_2$	8.7×10^{-8}	0	Dissociative recombination
46	$F^- + CF_3^+ \rightarrow CF_2 + F + F$	$3.0 \times 10^{-7} \times (T/298.)^{-0.5}$	0	Dissociative recombination
47	$F^- + CF_3^+ \rightarrow CF_3 + F$	3.0×10^{-7}	0	Recombination

48	$F^-+CF_2^+ \rightarrow CF+F_2$	9.1×10^{-8}	0	Dissociative recombination
49	$F^-+CF_2^+ \rightarrow CF_2+F$	5.0×10^{-7}	0	Recombination
50	$F^-+CF^+ \rightarrow CF+F$	9.8×10^{-8}	0	Recombination
51	$F^-+CF^+ \rightarrow C+F+F$	$7.0 \times 10^{-7} \times(T/298.)^{-0.5}$	0	Dissociative recombination
52	$F^-+F_2^+ \rightarrow F+F_2$	9.4×10^{-8}	0	Recombination
53	$F^-+F^+ \rightarrow F+F$	7.1×10^{-7}	0	Recombination
54	$CF_3^-+CF_3^+ \rightarrow CF_3+CF_3$	3.0×10^{-7}	0	Recombination
55	$CF_3^-+CF_2^+ \rightarrow CF_3+CF_2$	5.0×10^{-7}	0	Recombination
56	$CF_3^-+CF^+ \rightarrow CF_3+CF$	7.0×10^{-7}	0	Recombination
57	$CF_3^-+F^+ \rightarrow CF_3+F$	7.0×10^{-7}	0	Recombination
58	$CF_3^-+F_2^+ \rightarrow CF_3+F_2$	5.0×10^{-7}	0	Recombination
59	$F^-+CF_3 \rightarrow CF_4+e$	4.0×10^{-10}	0	Detachment
60	$F^-+CF_2 \rightarrow CF_3+e$	3.0×10^{-10}	0	Detachment
61	$F^-+CF \rightarrow CF_2+e$	2.0×10^{-10}	0	Detachment
62	$F^-+C \rightarrow CF+e$	1.0×10^{-10}	0	Detachment
63	$F^-+F \rightarrow F_2+e$	1.0×10^{-10}	0	Detachment
64	$F^-+C_2F_5^+ \rightarrow F+C_2F_5$	8.0×10^{-8}	0	Recombination
65	$F^-+C_2F_4^+ \rightarrow CF+CF_2+F_2$	8.2×10^{-8}	0	Dissociative recombination
66	$F^-+C_2F_3^+ \rightarrow F+C_2F_3$	8.0×10^{-8}	0	Recombination
67	$CF_3^-+C_2F_5^+ \rightarrow CF_3+C_2F_5$	1.0×10^{-7}	0	Recombination
68	$CF_3^-+C_2F_4^+ \rightarrow CF_3+C_2F_4$	1.0×10^{-7}	0	Recombination
69	$CF_3^-+C_2F_3^+ \rightarrow CF_3+C_2F_3$	1.0×10^{-7}	0	Recombination
70	$CF_3+CF_3^- \rightarrow C_2F_6+e$	1.0×10^{-10}	0	Electron detachment

[a]The unit of the rate coefficient is cm^3s^{-1} for the two-body reactions. The letter c means that the rate coefficient is calculated from the electron energy transport module based on the corresponding electron impact cross sections.

[b]According to experiments[37], the parent or non-dissociative attachment of low energy electrons with C_4F_8 proceeds in two steps, i.e., first formation of excited negative ions ($C_4F_8^{-*}$, for which the internal excitation energy is larger than the electron affinity), followed by relaxation to ground state $C_4F_8^-$ by collision with heavy neutral species. These two steps are represented in our reaction set by Nos. 8 and 43, respectively.

[c]The lifetime of $C_4F_8^{-*}$ for autodetachment was measured as 10μs using time-of-flight mass spectrometry[13]. Thus we estimated the rate coefficient of this process as 10^5 s^{-1}.

III. Results and Discussion

In section III.1, the calculated total and individual anion densities as a function of power, at a pressure of 10, 30 and 50mTorr, are analyzed.

Subsequently, the underlying mechanisms determining the anion behavior, i.e., the availability of feedstock molecules and the electron kinetics, are discussed in section III.2. Next, the importance of parent and dissociated negative ions at different discharge conditions is identified in section III.3. Finally, a detailed comparison of our simulation results with existing experimental data is presented in section III.4.

III.1 Variation of negative ion densities with power and pressure

In Fig.3, the total negative ion density, and the densities of the main negative ions, i.e., the excited $C_4F_8^{-*}$ ions, the ground-state $C_4F_8^-$ ions, and the F^- ions, are plotted versus power, at 10, 30 and 50mTorr. As seen in Fig. 3(a), at 30mTorr, the total negative ion density first increases with power and then decreases. At lower pressure (~10mTorr), the non-monotonic trend is also visible, but the maximum density moves significantly to lower power values. At higher pressure (~50mTorr), the density continuously increases with power, i.e., the maximum is not yet reached within the power range under study. The experimentally observed non-monotonic variation of negative ion density with power at 10mTorr[19, 20] is correctly predicted by the model. Moreover, the continuously increasing anion density with power at 50mTorr is similar to the behavior observed in fc ccp sources, in C_4F_8, CF_4, CHF_3, C_2F_6, and C_3F_8, under similar discharge conditions (~100mTorr)[17, 18].

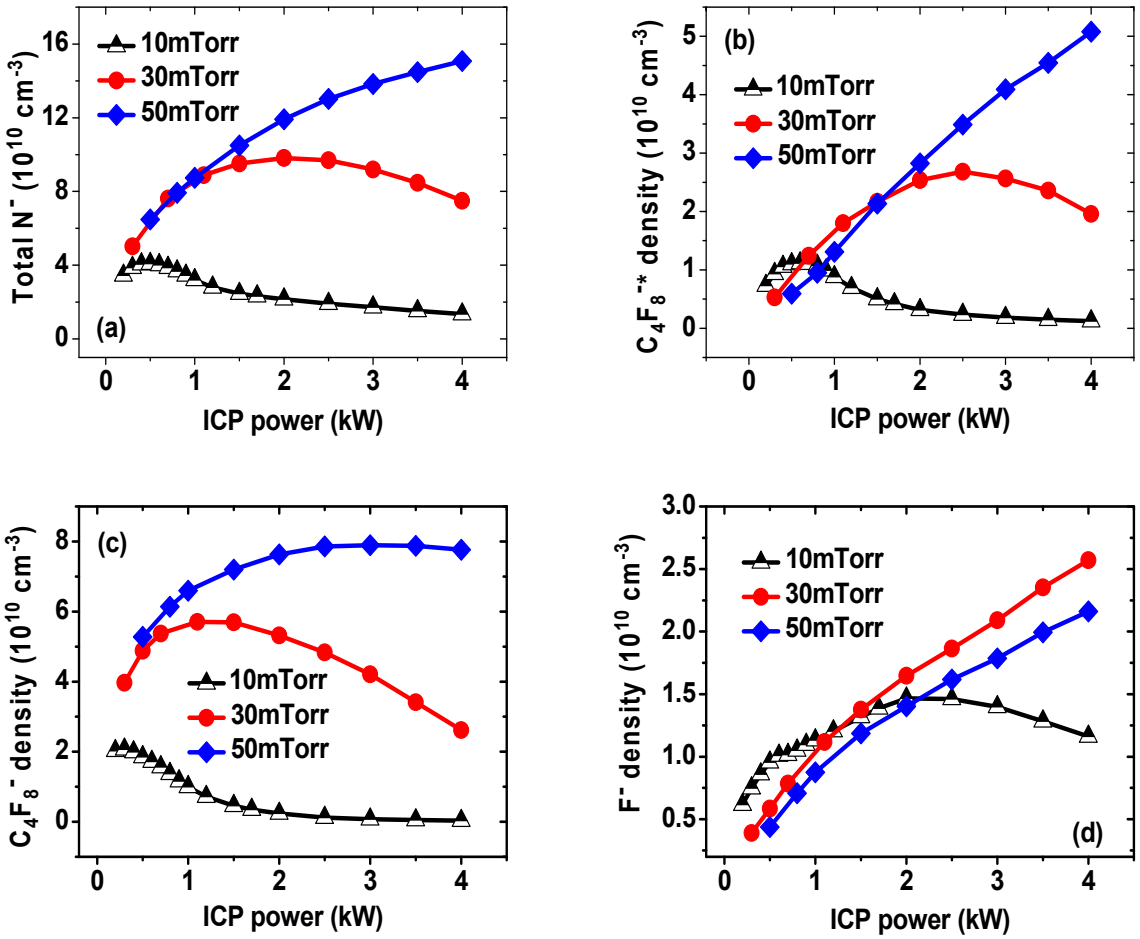

Figure 3. Total negative ion density (a), $C_4F_8^{-*}$ density (b), $C_4F_8^-$ density (c), and F^- density (d) versus power at three different gas pressures. The densities of all negative ions are spatially averaged.

From Fig. 3(b) it is clear that the $C_4F_8^{-*}$ density varies with power in almost the same way as the total negative ion density of Fig. 3(a), at the three different pressures. It indicates that in C_4F_8 ICP sources, the excited parent anions predominantly determine the variation of the total negative ion density. This is because, as mentioned in refs. [12-14], for large-size fc molecules, like C_4F_8, the cross section for parent attachment is higher than for dissociative

attachment, as compared with smaller fc molecules, like CF_4 and C_2F_6. This behavior was also reported by Kono *et al*[17], who predicted that in a C_4F_8 ccp source at low power and large availability of feedstock gas, the heavy negative ions, probably the parent anions, dominate. Moreover, it is well known that the residence time of the feedstock gas in an ICP reactor (i.e., around 100s of ms) is longer than in a ccp (i.e., typically $\leq$10 ms), as the ICP reactor size is larger[38-40]. Thus, the electrons will have more chance for directly colliding with background C_4F_8 molecules, which enhances even the production of parent anions.

As appears from Fig. 3(c), the trend of the $C_4F_8^-$ ground state density with power at the three pressures is basically the same as for the excited $C_4F_8^{-*}$ anions. Nevertheless, the variation of the $C_4F_8^-$ density is always ahead of the $C_4F_8^{-*}$ density. In particular, at 30 mTorr, the peak of the $C_4F_8^-$ density appears at a lower power value (1-1.5kW) than for the $C_4F_8^{-*}$ density (2.5kW). This is because the $C_4F_8^-$ ions are exclusively produced by de-excitation of $C_4F_8^{-*}$, and thus their density evolution will be naturally limited by the concentration of their precursor, $C_4F_8^{-*}$. Besides, the $C_4F_8^-$ densities are somewhat higher than the $C_4F_8^{-*}$ densities. This is because the rate of $C_4F_8^{-*}$ de-excitation (reaction No. 43 in Table 4) is quite high, due to the high density of the reactant M, i.e., the sum of all fc neutrals (including C_4F_8), thus leading to a strong transfer of $C_4F_8^{-*}$ to $C_4F_8^-$. However, in spite of its lower density, $C_4F_8^{-*}$

still determines the trend of the total anion density with power, because it is the precursor of $C_4F_8^-$. Therefore, in Sec. III B, the production mechanisms of $C_4F_8^{-*}$, and not of $C_4F_8^-$, will be analyzed.

Fig. 3(d) shows that the F^- density continuously increases with power at 30 and 50mTorr, while at 10mTorr, it goes over a maximum at a certain power, although this power value is much higher than for the parent anions. The F^- ions can be produced by electron dissociative attachment to both C_4F_8 and fragmented fc neutrals. At high pressure, the continuous increase of the F^- density is due to higher production of dissociated fc neutrals with power. The non-monotonic variation of the F^- density at low pressure indicates that both C_4F_8 and the fc neutrals are depleted by ionization.

III.2 Production of the negative ions

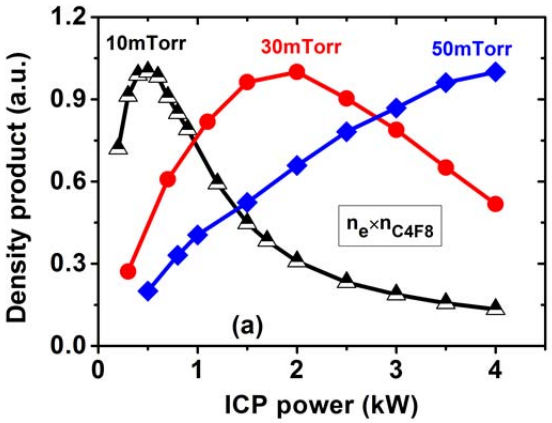

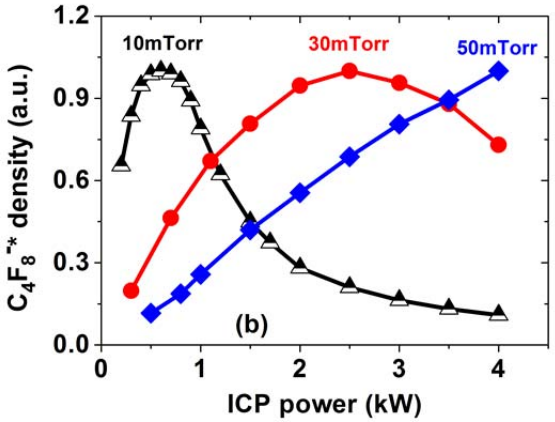

Figure 4. (a) Product of electron and C_4F_8 densities, $n_e \times n_{C4F8}$, and (b) $C_4F_8^{-*}$ density versus power at 10, 30 and 50mTorr, both in arbitrary units and spatially averaged. The maxima of the density products at 10, 30, and 50mTorr are 2.44×10^{24}, 1.80×10^{25}, and 5.51×10^{25} cm^{-6}, respectively. The $C_4F_8^{-*}$ density maxima are 1.11×10^{10}, 2.68×10^{10} and 5.079×10^{10} cm^{-3}, respectively. However, all maxima are here set equal to 1, to allow the best comparison of the profiles.

As mentioned before, the excited $C_4F_8^{-*}$ ions determine the total negative ion behavior with power. Hence, we discuss here the production mechanism of this species. We know that the $C_4F_8^{-*}$ ions are exclusively produced by parent attachment of electrons with feedstock C_4F_8 molecules; see reaction No. 8 in Table 4. Thus, the density product of electrons and C_4F_8 molecules will determine the $C_4F_8^{-*}$ density. Therefore, we plot in Fig. 4(a) this density product against power at the three different pressures, with their maxima set equal to 1. To facilitate the analysis, the $C_4F_8^{-*}$ densities, also normalized, are

plotted in Fig. 4(b) for comparison. It is clear that the trends in both figures are very similar. There are only some small differences, e.g., at 30mTorr, the $C_4F_8^{-*}$ density has its maximum at 2.5kW, while the density product peaks at 2.0kW. The non-monotonic variation as a function of power for the (spatially averaged) density product at 10 and 30 mTorr can be clarified based on the evolution of its spatial profile with power.

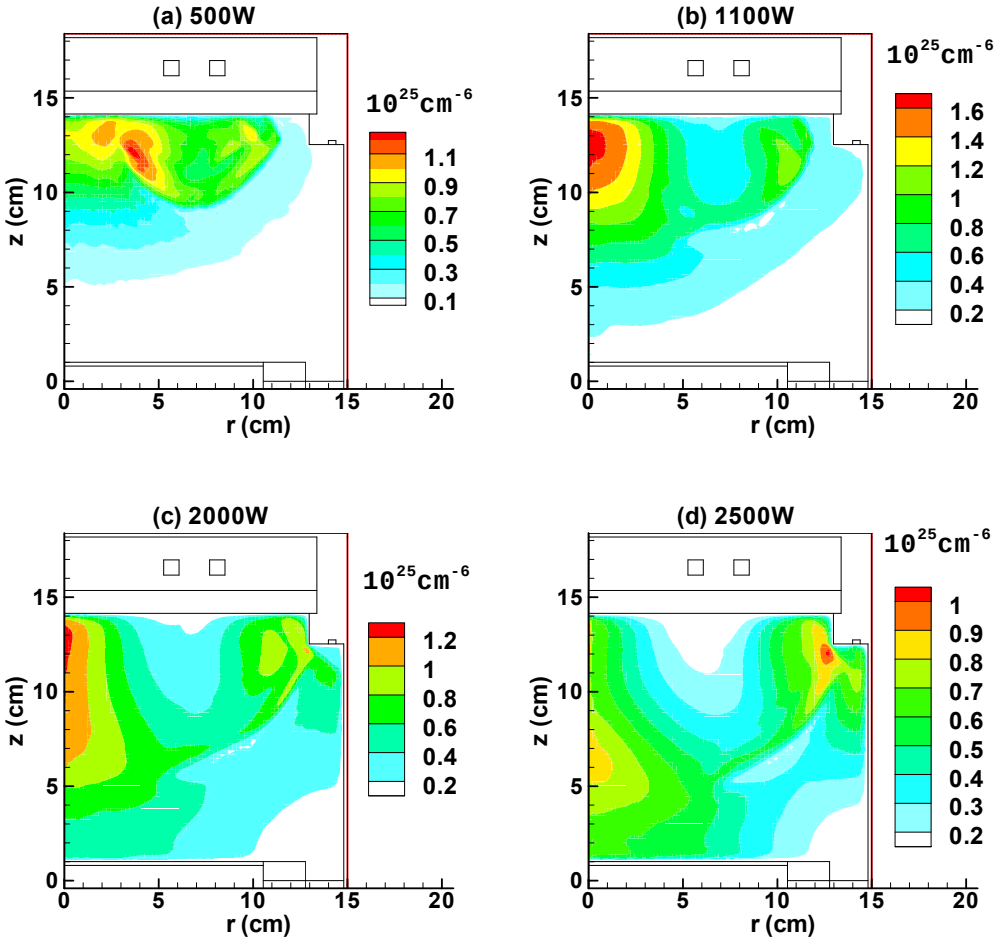

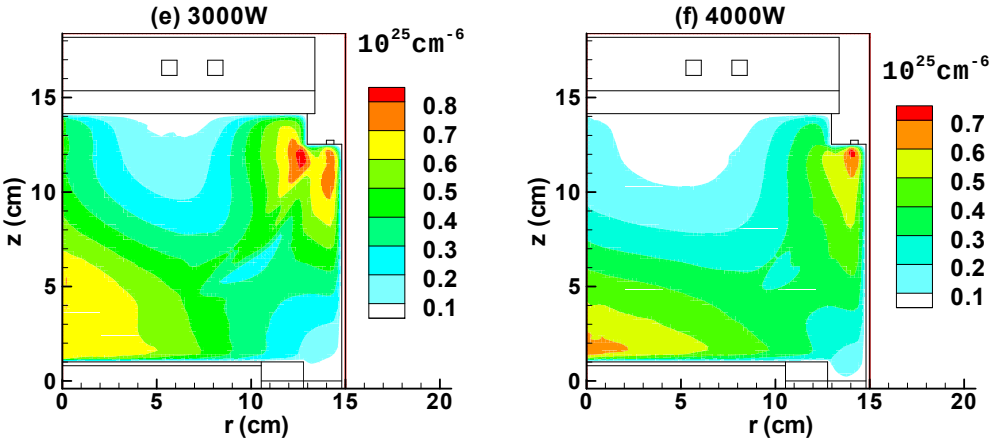

Figure 5. Spatial profiles of the density product of electrons and feedstock C_4F_8 molecules, $n_e \times n_{C4F8}$, at different power values. The pressure is fixed at 30mTorr.

Fig. 5 illustrates the product of electron and C_4F_8 density profiles at different power values and a fixed pressure of 30mTorr. The product first increases up to 1100W and then begins to drop. At the same time, the spatial profile of the product changes significantly. At low power, like 500W, the product reaches its maximum under the dielectric window. When increasing the power up to 2000W, the peak shifts toward the axis center, and a secondary peak arises near the reactor sidewall, or more specifically near the gas inlet. Upon further increasing the power, the central peak moves downward from the dielectric window toward the reactor bottom, while the secondary peak near the gas inlet becomes more pronounced, and a minimum is reached in the heating area under the dielectric window. The latter is attributed to severe depletion of the C_4F_8 gas molecules, which are more efficiently converted into reactive

species (radicals, ions) upon increasing power. This depletion cannot be counteracted by the increased electron density. Thus we can conclude that at low power, when the C_4F_8 depletion is negligible, the $C_4F_8^{-*}$ density increases with power, because of the increasing electron density, while at high power, the higher amount of electrons produced cannot counteract the C_4F_8 depletion, thus resulting in a decreasing $C_4F_8^{-*}$ density. This explains the non-monotonic variation of the negative ion density with power at 30 mTorr. The same explanation also holds true at other pressures, but the power value at which the maximum negative ion density is reached, and hence which marks the threshold for significant C_4F_8 depletion, increases with pressure, which is logical. This mechanism, predicted by the model, corresponds with the explanation proposed by Hebner *et al* in ref. [19], but our model gives more details on the mechanism of how the potential anion precursor species, here the feedstock C_4F_8 molecules, influence the negative ion density.

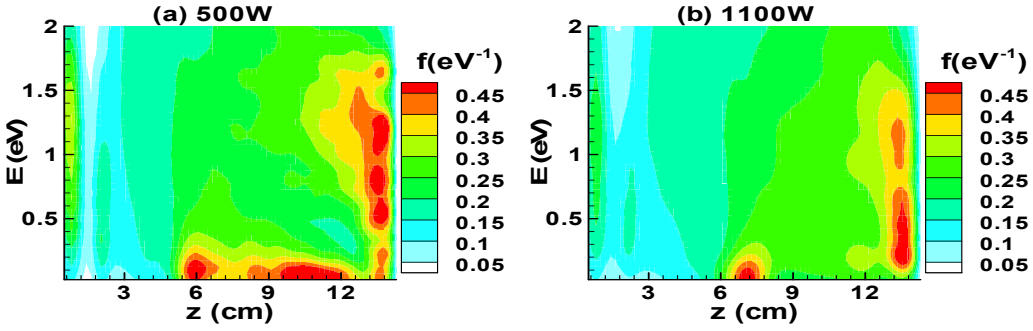

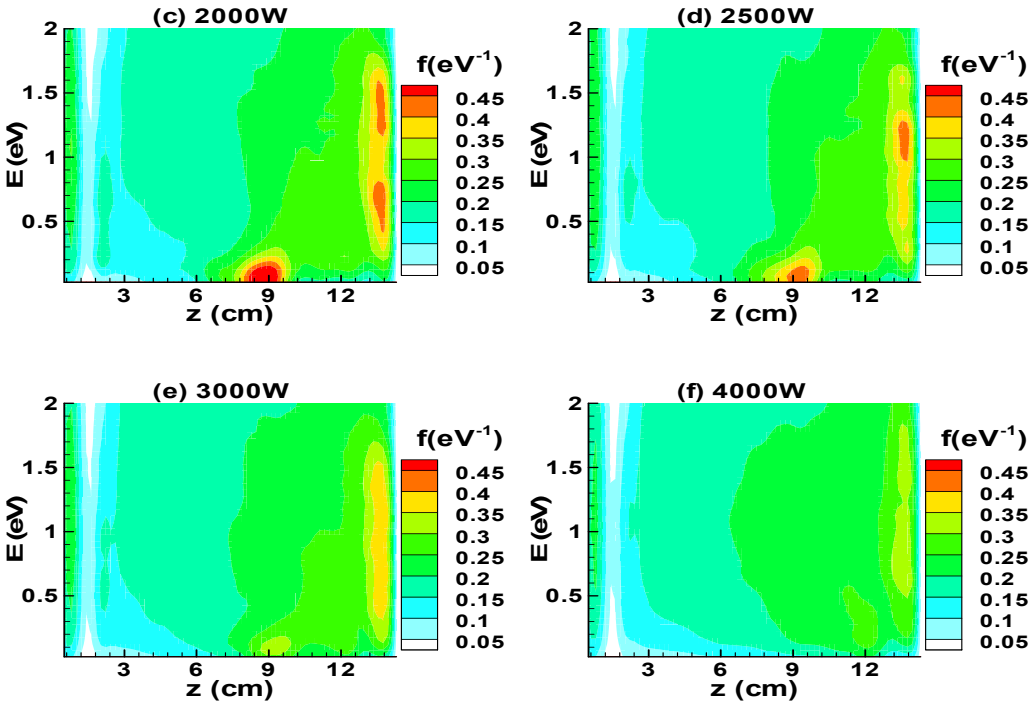

Figure 6. Electron energy distribution functions in the low energy range (0-2eV), averaged over the radial distance, as a function of axial position (z) at different ICP powers. The pressure is fixed at 30mTorr.

As illustrated in Tables 1-3, many electron impact vibrational excitations exist, for both the feedstock and the fragmented fc molecules. It is known that these reactions consume a considerable fraction of the deposited power, by forming low energy electrons, and the appearance of the low energy electrons may influence the negative ion behaviour since the anions are produced by low energy electrons. Therefore, in Fig. 6, we plot the spatially resolved electron energy distribution functions (eedfs) for the same power values as in Fig. 5, in the low energy range of 0-2eV, at 30mTorr. Note that these distribution functions are averaged along the radius, and thus only the axial variation is shown.

It is seen that at low power (500W) a substantial fraction of low energy electrons exists, and they can be classified into two groups according to their energy and spatial location. The electrons with very low energies, less than 0.2eV, are situated in the bulk plasma, while the electrons with wider energy distribution are found in the heating region below the coil. Apparently, they are formed by different mechanisms. The bulk plasma low energy electrons are formed because at such low power, the discharge is more localized (cf. Fig. 10(a)), and hence the energy losses of the bulk electrons through vibrational excitation cannot be effectively compensated by the power source. The low energy electrons in the heating region, on the other hand, are formed by various inelastic electron collisions with high energy thresholds.

Upon increasing the power, the proportions of the two groups of low energy electrons are both reduced, due to the effect of discharge expansion, which will be revealed in Sec. III.3, as well as due to the high deposited power density. Naturally, the presence of low energy electrons is helpful for the production of negative ions at low powers, especially for the parent anion production. This may explain why, at 10 and 30mTorr, the power range in which the $C_4F_8^{-*}$ density increases is wider than the range of the product of electron and C_4F_8 densities, as demonstrated in Fig. 4. Note that upon increasing the power, the absolute electron density increases, resulting also in

an increase of low energy electrons, and this effect can perhaps dominate over the decrease in the proportion of the eedfs caused by the high power density, as mentioned above.

III. 3 Negative ion identification

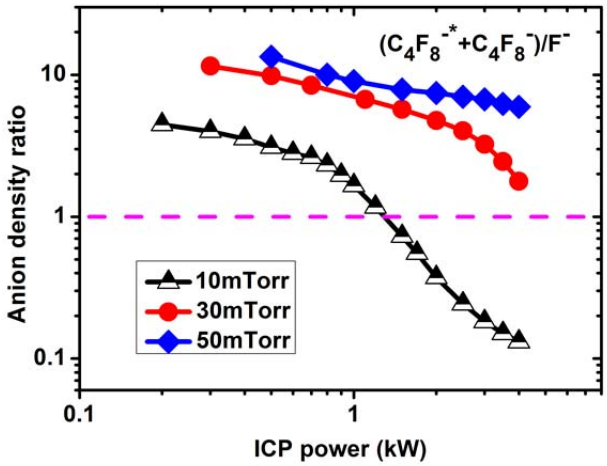

Figure 7. Density ratio of the parent anions, i.e., the sum of the $C_4F_8^{-*}$ and $C_4F_8^-$ ions, to the F^- ions, as a function of ICP power, at 10, 30 and 50 mTorr. The densities used to calculate the ratio are spatially averaged values.

In this section, we identify the importance of the different negative ions. The calculated CF_3^- anion density is one order of magnitude lower than the F^- density, since there are more F^- production channels (Nos. 1, 3, 4, 6 and 9 in Table 4) than CF_3^- production channels (Nos. 2, 5 and 7). Moreover, the cross sections of F^- production (e.g., reaction No. 1) are three or four times higher than for CF_3^- production (e.g., reaction No. 2)[41], and finally, the F^- ions can directly be produced from the feedstock gas (C_4F_8; see reaction No. 9), which

typically has a higher density than the other precursor molecules. Furthermore, in the experiments performed for C_4F_8 plasmas, the cross sections for the middle mass negative ion production, like $C_2F_x^-$ and $C_3F_x^-$, were found to be about two orders lower than for the production of F^- and heavy parent anions[12]. Hence for simplicity, these anions were not included in our present model. Therefore, in this section, only the excited $C_4F_8^{-*}$ ions, ground-state $C_4F_8^-$ ions and dissociated F^- ions are considered.

Thus, these main negative ions are classified into two types, being (i) the heavy parent anions, i.e., the sum of $C_4F_8^{-*}$ and $C_4F_8^-$, and (ii) the light dissociated anion, F^-. The density ratio of the sum of both parent anions over F^-, at the three pressures under study, is plotted vs power in Fig. 7. In most cases, especially at the pressures of 30 and 50mTorr, the heavy anions are dominant over the light F^- ions, with a density being up to 10 times higher. However, at higher power, the difference in densities is reduced for the three different pressures investigated, and at 10mTorr and a power $\geq$1200W, when the C_4F_8 molecules become significantly depleted, the F^- ions become more important than the parent anions.

To explain the trends in the different anion compositions, we plot in Figs. 8 and 9 the spatial profiles of the sum of the $C_4F_8^{-*}$ and $C_4F_8^-$ densities (i.e., the parent anions), and the F^- density, respectively, at 30mTorr. As seen in Fig. 8,

at low powers, i.e., 500W and 1100W, the sum of the parent ion densities is high in the heating region, i.e., under the dielectric window. However, at high powers, i.e., 2000W and 3000W, the parent anion densities are high in the downstream part of the chamber, and they reach a minimum in the heating region. This can be explained from the precursor molecules, i.e., C_4F_8, which become more and more depleted under the dielectric window at high power (see above and see also Fig. 10 below).

From Fig. 9, on the other hand, it is clear that the F^- ion densities peak under the dielectric window at all powers investigated, but upon increasing power, the density distribution becomes more smooth. This is caused by the characteristic electron density profile, shown in Fig. 10, which expands towards the downstream chamber due to the C_4F_8 depletion. Indeed, as mentioned above, both the feedstock C_4F_8 molecules and the fragmented fc (C_xF_y) species can produce F^- ions, by electron dissociative attachment. Upon higher power, the feedstock molecules are depleted, while the fragmented C_xF_y species become more important and take the role as precursors for F^- production. It is well known that the C_xF_y species, like the fc ions, are mainly produced in the heating region, i.e., under the dielectric window, since the thresholds of electron impact dissociation are high and dissociation is thus caused by high energy electrons. Thus, we can conclude that because of the occurrence of various F^- production reactions and hence the sufficient supply

of reactant species (first C_4F_8 and at higher power C_xF_y), an expanding electron density profile with power will cause an expanding F^- density profile, since the F^- production is determined by the electron profile, rather than being precursor-limited.

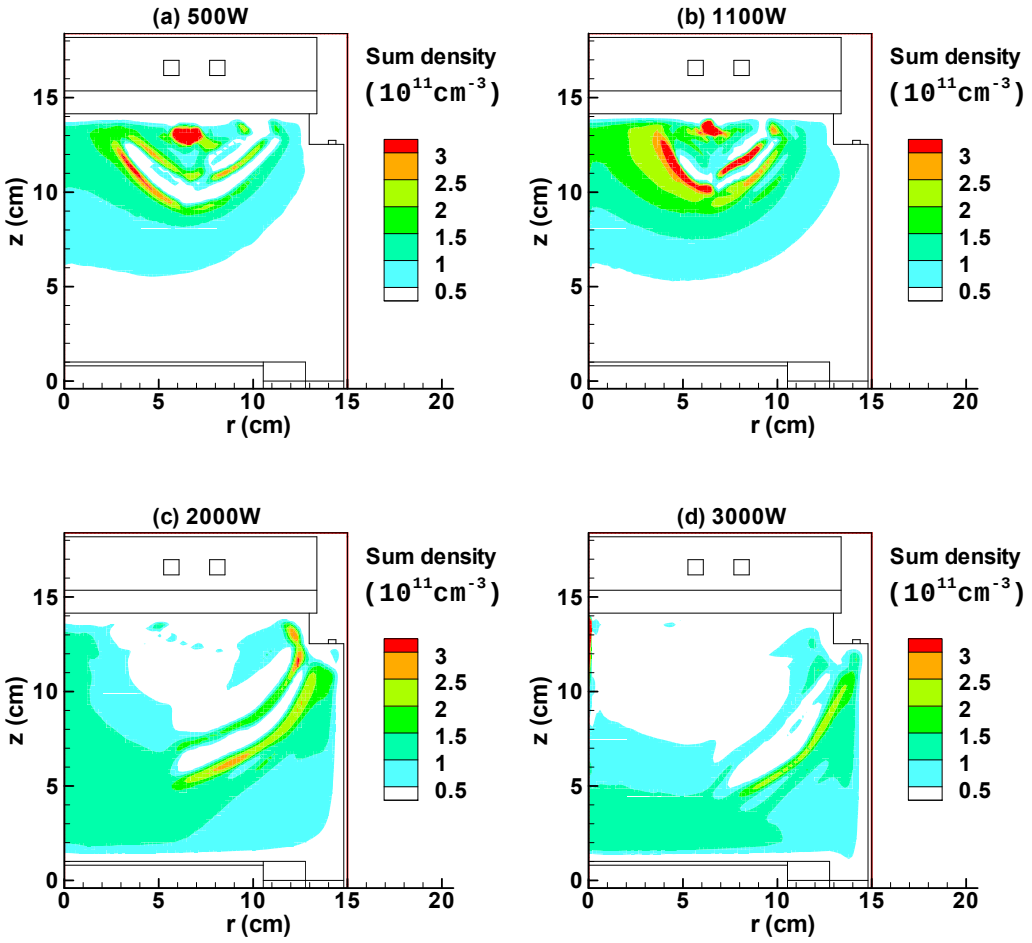

Figure 8. Spatial profiles of the sum of the $C_4F_8^{-*}$ and $C_4F_8^-$ ion densities, at 500W, 1100W, 2000W and 3000W. The pressure is fixed at 30mTorr.

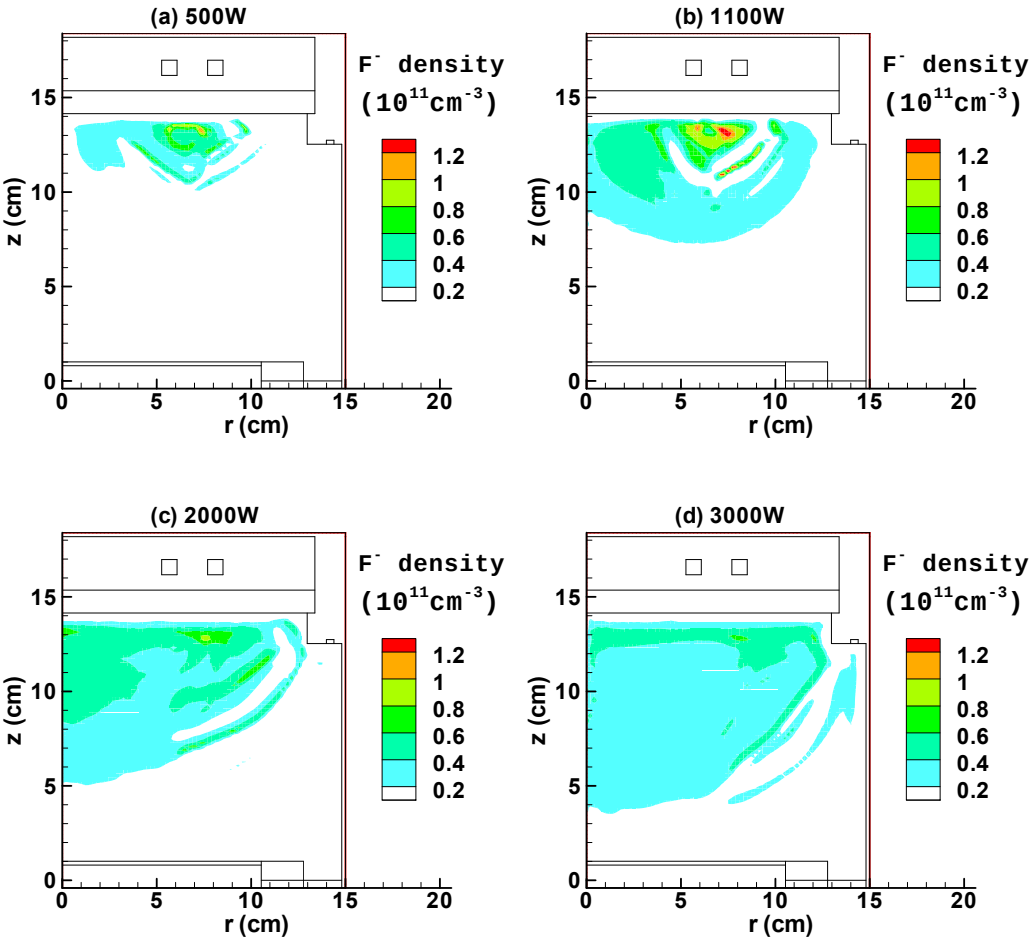

Figure 9. Spatial profiles of the F^- density at 500W, 1100W, 2000W and 3000W. The pressure is fixed at 30mTorr.

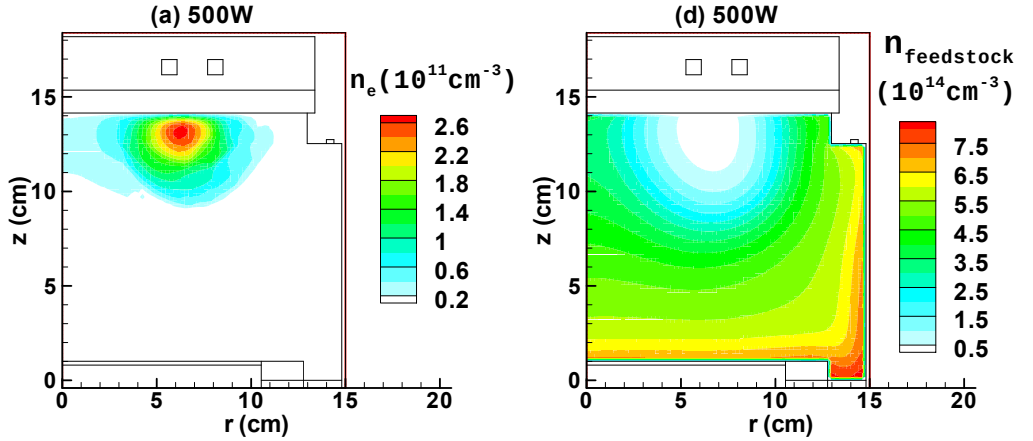

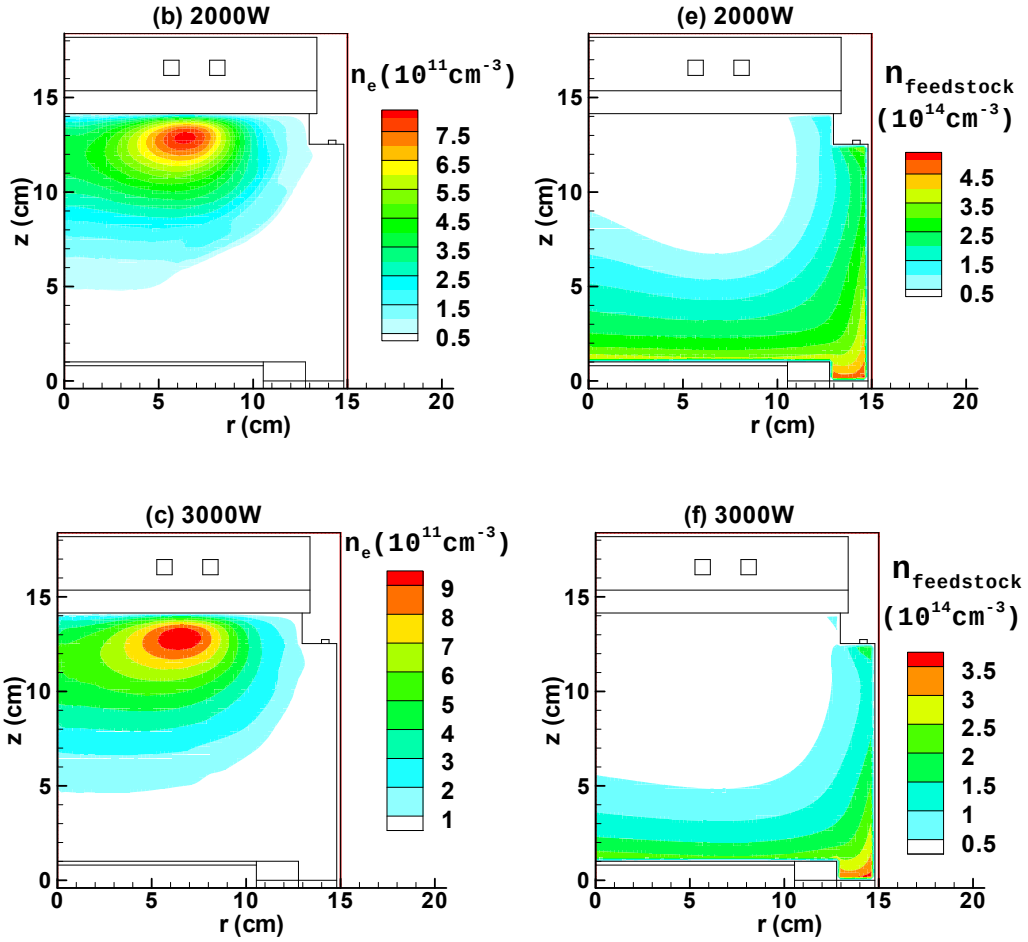

Figure 10. Spatial profiles of the electron density n_e (a-c) and the C_4F_8 density $n_{feedstock}$ (d-f) at 500W, 2000W and 3000W. The pressure is fixed at 30mTorr.

The maximum of the parent anion density (cf. Fig. 8) is only 2.5 times the maximum F^- ion density (cf. Fig. 9); however, the difference is much larger when comparing the spatially averaged values; cf. Fig. 7 above. Indeed, the F^- ion density shows a very local maximum, whereas the sum of the parent anion densities is more spread out in the entire reactor, especially at low powers. This is again because of the large height of the ICP reactor, where the downstream volume temporarily stores the C_4F_8 molecules for parent

attachment. This effect is more pronounced at high pressure, like 50mTorr; cf. Fig. 7. This is quite different with the case of a thin-sheet CCP source. Indeed, in C_4F_8 CCPs, it was found that in most discharge conditions (except for the very low power case[17]), the light F^- ions dominate in the anion composition[42]. Our simulations reveal that the short axial distance of the CCP reactor, together with the short residence time, should be responsible for the difference in the anion composition of C_4F_8 sources, due to the lack of storage possibilities for C_4F_8, especially in the downstream chamber part.

At low pressure, i.e., 10mTorr, the parent anions are still predominant at low power, i.e., $\leq$1100W, but at high power, the spatially averaged F^- density becomes larger than the parent ion density, as is clear from Fig. 7. This is because the C_4F_8 molecules are now consumed in the entire chamber and the anions are now mainly produced by electron dissociative attachment on C_xF_y fragments, producing thus mainly F^- ions.

III. 4 Validation of the simulations

It should be noted that the above analysis with respect to the non-monotonic anion density in our simulation is based on the spatially averaged values. However, the experimental data related to this behavior were obtained at specific locations. So, to validate our simulations in more detail, in this section we compare the negative ion density with experimental data at similar

conditions, although it should be realized that the reactor size in our work is larger than in the experiment in Ref. [19], and our range of power values is also larger. More specifically, the ICP reactor in the experimental setup of Ref. [19] has a height of 3.8 cm and a radius of 5.5 cm, yielding a volume of about 361cm³ or 0.361L. In our simulations, the reactor height and radius are both 15cm, yielding a volume of about 10.6L. The power in Ref. [19] is in the range of 0.1 – 2 kW, while it is 0.2 – 4 kW in our simulations. Thus the power density in Ref. [19] is in the order of 0.3-1.1 kW/L, which is higher than in our simulations (0.02-0.38 kW/L). On the other hand, the calculated mean free path of electrons (about 0.13 cm) and ions (about 0.72 cm) in the background gas C_4F_8 are much smaller than the chamber dimensions, in both our simulations and the experiments, so the main heating mechanism in both cases is Ohmic heating. To conclude, the comparison of the two sets of data, even probed at the same spatial location, is still only based on roughly the same condition. However, we do not expect that this difference influences the final conclusion to a large extent, as analyzed below.

To allow a better comparison with the experiment[19], we focus on the simulated anion density profiles at 10mTorr, from which the densities of the individual anions, the total anion and electron density at the position of 1cm above the wafer are probed. These results are plotted in Fig. 11. Note that the non-monotonic variation of the total anion density with power at roughly the

same conditions is indeed captured by the model, even though some differences between the simulated and experimental curves are observed. In particular, the experimental total negative ion density is somewhat higher than the calculated value. Moreover, the experimental negative ion density is symmetric relative to its maximum, which is more consistent with the spatially averaged anion density as illustrated in Fig. 3(a). We believe that the differences are caused by the larger reactor used in our work, as compared with Ref. [19]. Naturally, the storage effect of feedstock gas in the ICP reactor, as revealed above, will be more important as the reactor becomes larger. Correspondingly, the spatial variation of the anion density will be more significant. This can somehow explain the asymmetric feature of the calculated total anion density. In other words, in a smaller reactor, the anion behavior at a certain position corresponds better with the volume averaged value. Finally, also the calculated and measured electron density variations as a function of power are very similar, although the absolute values are clearly different, which is again attributed to the larger reactor size in the calculations.

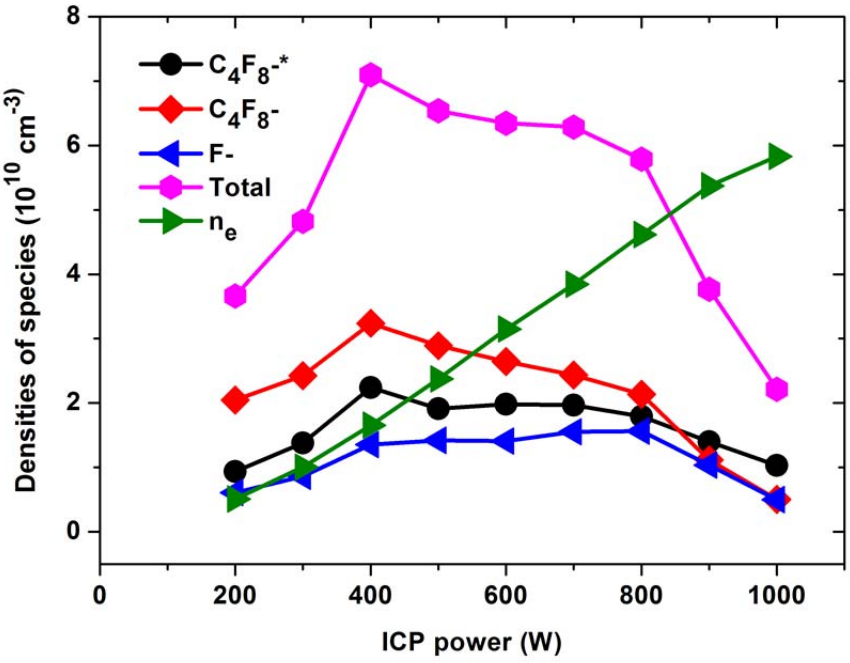

Figure 11. Calculated densities of individual anions, as well as the total anion and electron density, probed at 1 cm above the wafer of the chamber, as a function of the ICP power, at 10mTorr.

IV. Conclusion

In this paper, the negative ion behavior in a C_4F_8 ICP source is investigated using a hybrid model. The total negative ion density and the densities of the main anions are presented as a function of the applied power at different pressures. The ground state $C_4F_8^-$ density is higher than the excited $C_4F_8^{-*}$ density, but as the $C_4F_8^{-*}$ ions are the precursors for the $C_4F_8^-$ ground state ions, they determine the general trend of the total anion behavior. The model predicts a non-monotonic variation of the total negative ion density at low and intermediate pressure (10-30 mTorr), which is in agreement with experiments

that were conducted in different fc plasma sources[19, 20]. This behavior is explained from the dominant source of excited $C_4F_8^{-*}$, i.e., electron parent attachment of C_4F_8. Indeed, the product of electron and C_4F_8 densities exhibits the same trend upon increasing power. The drop in negative ion density with power above a certain power value is caused by the depletion in the feedstock C_4F_8 molecule density, which is not compensated by the higher electron density. At low pressure, the C_4F_8 depletion is more pronounced, and thus the $C_4F_8^{-*}$ (and total negative ion) density peaks at lower power. At high pressure (50mTorr), the $C_4F_8^{-*}$ (and total negative ion) density monotonically increases with power within the investigated power range, which is similar to fc ccp sources. Besides, the role of the electron kinetics in determining the anion behavior is discussed, and it is found that the presence of low energy electrons by vibrational excitation enhances the anion production at low power. Furthermore, the negative ion composition is identified in this paper. The parent anion densities (i.e., the sum of $C_4F_8^{-*}$ and $C_4F_8^{-}$) are typically up to one order of magnitude higher than the F^- density, especially at high pressure (30-50 mTorr), but the difference becomes smaller at higher power. The dominance of parent anions is because of the larger ICP reactor size, enabling to store the C_4F_8 precursor molecules. This is quite different with the C_4F_8 CCP case where the light F^- ions are more predominant. Only at low pressure (10mTorr) and high power, the F^- ions become dominant. This is because in this special case, the C_4F_8 molecules are depleted in the whole chamber

volume. Finally, a detailed comparison of our simulation results with the experiments at roughly the same conditions is illustrated.

APPENDIX: MAIN EQUATIONS APPLIED IN THE HYBRID MODEL

Here we present the main equations that are used in the three basic modules of the hybrid plasma equipment model (HPEM).

1. Fluid Kinetics Module

In the fluid kinetics simulation, the mass, momentum and energy conservation equations of all charged and neutrals species are solved. The electron, ion and neutral equations are given separately. Besides, the electrostatic fields that are produced by the net spatial charge density are calculated by the Poisson equation.

1.1 Electron equations

$$\frac{\partial n_e}{\partial t} + \nabla \cdot \mathbf{\Gamma}_\mathbf{e} = R_e, \tag{A1}$$

$$\mathbf{\Gamma}_\mathbf{e} = -\frac{\nabla(n_e k T_e)}{m_e \nu_{en}} - \frac{e n_e}{m_e \nu_{en}} \mathbf{E}_s, \tag{A2}$$

The electron mass and momentum equations are expressed in Eqs. (A1-A2). The electron energy equation is not included here since the electron temperature is calculated directly in the Monte Carlo module. Due to the low mass, the drift-diffusion approximation is used for the momentum equation. Here n_e is the electron density, Γ_e is the electron flux density, m_e is the electron mass, T_e is the electron temperature, k is the Boltzmann constant,

ν_{en} is the electron collision frequency with neutrals, E_s is the electrostatic field, and R_e is the source term of electron density.

1.2 Ion equations

$$\frac{\partial n_i}{\partial t} + \nabla \cdot n_i \mathbf{u}_i = R_i, \tag{A3}$$

$$\frac{\partial n_i m_i \mathbf{u}_i}{\partial t} + \nabla \cdot (n_i m_i \mathbf{u}_i \mathbf{u}_i) = -\nabla (k n_i T_i) + e n_i \mathbf{E}_s - \mathbf{M}_i, \tag{A4}$$

$$\frac{\partial (n_i c_i T_i)}{\partial t} + \nabla \cdot (n_i \mathbf{u}_i c_i T_i) = \nabla \cdot \kappa \nabla T_i - P_i \nabla \cdot \mathbf{u}_i + \frac{n_i q_i^2 \nu_i}{m_i (\nu_i^2 + \omega^2)} E_\theta^2 + \frac{n_i q_i^2}{m_i \nu_i} E_s^2 + E_i, \tag{A5}$$

For the ions, the full set of conservation equations for mass, momentum and energy are used, as shown in Eqs. (A3-A5). In the momentum equation, Eq. (A4), besides for the inertia term and convective term at the left hand side, the pressure gradient, electrostatic field acceleration, and momentum transfer due to collisions with other species are included in the right hand side (rhs). Here the expression of M_i is $\sum_n \frac{m_n}{m_i + m_n} n_i n_n (\bar{\upsilon}_i - \bar{\upsilon}_n) \nu_{in}$, where the sum is based on all considered neutral species n, m_i and m_n are the masses of the ion and neutral, n_i and n_n are the densities of the ion and neutral, $\bar{\upsilon}_i$ and $\bar{\upsilon}_n$ are the mean speeds of the ion and neutral, and ν_{in} is the elastic collision frequency between the ion and the neutral. For the energy equation, Eq. (A5), the first and second terms of the rhs denote the thermal conductivity and compressive heating. The Joule heating from the electromagnetic field and electrostatic field are also considered for the ions, and they are represented by the third and fourth terms of the rhs, repectively. The final term of Eq. (A5)

represents the energy transfer caused by the elastic collisions and the charge exchange collisions of ions with other particles. Here the expression of E_i is $\sum_n 3\frac{m_n}{m_i+m_n} n_i n_n k(T_n - T_i)\nu_{in} - \sum_n 3 n_i n_n R_{in} k T_i$, where T_i and T_n are the temperature of the ion and neutral, k is the Boltzmann constant, and R_{in} is the charge exchange collision frequency between the ion and the neutral. The other variables have the same meaning as above. For more details of the expressions of M_i and E_i, we refer to Ref. [23].

1.3 Neutral equations

$$\frac{\partial n_n}{\partial t} + \nabla \cdot n_n \mathbf{u}_n = R_n, \tag{A6}$$

$$\frac{\partial n_n m_n \mathbf{u}_n}{\partial t} + \nabla \cdot (n_n m_n \mathbf{u}_n \mathbf{u}_n) = -\nabla(k n_n T_n) - \nabla \cdot \vec{\pi} + \mathbf{M}_n, \tag{A7}$$

$$\frac{\partial (n_n c_n T_n)}{\partial t} + \nabla \cdot (n_n \mathbf{u}_n c_n T_n) = \nabla \cdot \kappa \nabla T_n + -P_n \nabla \cdot \mathbf{u}_n + E_n, \tag{A8}$$

For the neutral kinetics, the same set of fluid equations, Eqs. (A6-A8), are used. However, due to the fact that the neutral densities are generally two orders higher than the ion densities, the viscous effect, represented by the second term of the rhs in Eq. (A7), is taken into account. Besides, the electrostatic field acceleration and the Joule heating term are excluded from the momentum and energy equations.

1.4 Poisson equation

$$\begin{aligned} \nabla^2 \varphi(r,z) &= -\frac{e}{\varepsilon_0}(n_i - n_e), \\ \mathbf{E}_s &= -\nabla \varphi, \end{aligned} \tag{A9}$$

The Poisson equation, Eq. (A9), is used to solve the electrostatic field caused by the net charge density. We used a constant mesh size of 0.2 cm in the axial and radial direction. This value is much larger than the Debye length, which is in the order of 0.002 cm at the conditions under study, but this is considered not to be a problem in hybrid models [43-46].

2. Electromagnetic Module

The inductively coupled plasma source can be performed in two modes, E and H modes. In this paper, only the H discharge mode, sustained by the azimuthal component E_θ , is considered. Moreover, the harmonic approximation is used, i.e., the temporal variations of the electromagnetic fields are in the form of $\exp(i\omega t)$. With this approximation, the whole set of Maxwellian equations, is reduced to a complex wave equation, i.e.,

$$\nabla^2 E_\theta(r,z) = i\omega\mu_0\sigma(r,z)E_\theta(r,z), \qquad \text{(A10)}$$

where E_Θ is the complex amplitude of the azimuthal component of the electric field. The amplitude is obtained by solving Eq. (A10) within the whole reactor using the method of successive-over-relaxation in cylindrical coordinates. The boundary conditions are obtained by assuming that the walls of the chamber and the wafer holder are perfectly metallic, while the reactor center is the symmetry axis.

3. Electron Monte Carlo Module

At the beginning of the MC simulation, the initial velocities of the simulated electrons are randomly selected from a Maxwellian distribution and the

simulated particles are stochastically distributed over the discharge region. The trajectories of the electrons are followed in the position and phase space according to Newton's laws by the inductive EM field and electrostatic field. The description of the electron-neutral collisions is based on the null collision technique. To speed up the numerical efficiency, the trajectories of each simulated particle are separately updated by the Newton's laws with individual timesteps. The statistics collected at each advancing step of all particles are used to calculate the EEDF at each position in the reactor. The spatial profiles of the transport and reaction rate coefficients, and of the electron temperature are all integrated from these EEDFs, as shown in Eq. (A11)

$$\begin{aligned} k_r(r,z) &= \int_0^\infty f(\varepsilon,r,z)\times\left(\frac{2\varepsilon}{m_e}\right)^{1/2}\sigma_r(\varepsilon)d\varepsilon, \\ T_e(r,z) &= \int_0^\infty f(\varepsilon,r,z)\times\varepsilon d\varepsilon, \end{aligned} \quad . \qquad \text{(A11)}$$

Acknowledgement

The work was conducted during a postdoc fellowship of S. X. Zhao at the University of Antwerp and was financially supported by the Belgian Federal Science Policy. Moreover, this work was also financially supported by the joint research project within the framework of the agreement between the Fund for Scientific Research Flanders (FWO) and MOST, by the National Natural Science Foundation of China (NSFC) (Grant Nos. 11075029 and

11305023), doctoral fund of Ministry of Education of China 20130041120054, and DUT13RC(3)19 foundation. The calculations were carried out using the Turing HPC infrastructure at the CalcUA core facility of the Universiteit Antwerpen, a division of the Flemish Supercomputer Center VSC, funded by the Hercules Foundation, the Flemish Government (department EWI) and the Universiteit Antwerpen.

Reference

[1] K. Ostrikov, I. B. Denysenko, S. Vladimirov, S. Xu, H. Sugai and M. Y. Yu, Physical Review E **67** (5), 056408 (2003).

[2] M. H. Anderson, S. Radovanov, L. S. Mock and P. J. Jesnick, Plasma Sources Science and Technology **3**, 302 (1994).

[3] S. Vladimirov, K. Ostrikov, M. Yu and G. Morfill, Physical Review E **67** (3), 036406 (2003).

[4] P. Chabert, H. Abada, J. P. Booth and M. A. Lieberman, Journal of Applied Physics **94** (1), 76 (2003).

[5] N. Nakano and T. Makaba, Journal of Physics D: Applied Physics **28**, 31 (1995).

[6] J. Schulze, A. Derzsi, K. Dittmann, T. Hemke, J. Meichsner and Z. Donkó, Physical Review Letters **107** (27), 275001 (2011).

[7] E. Stoffels, W. W. Stoffels and G. M. W. Kroesen, Plasma Sources Science and Technology **10**, 311 (2001).

[8] H. Ohtake and S. Samukawa, Applied Physics Letters **68** (17), 2416 (1996).

[9] W. W. Stoffels, E. Stoffels and K. Techibana, Japanese Journal of Applied Physics **36**, 4638 (1997).

[10] J. L. Jauberteau, G. J. Meeusen, M. Haverlag, G. M. W. Kroesen and F. J. de Hoog, Applied Physics Letters **55** (25), 2597 (1989).

[11] A. Kono and K. Kato, Applied Physics Letters **77** (4), 495 (2000).

[12] L. G. Christophorou and J. K. Olthoff, Journal of Physical and Chemical Reference Data **30** (2), 449 (2001).

[13] I. Sauers, L. G. Christophorou and J. G. Carter, The Journal of Chemical Physics **71** (7), 3016 (1979).

[14] S. R. Hunter and L. G. Christophorou, The Journal of Chemical Physics **80** (12), 6150 (1984).

[15] A. Kono, M. Haverlag, G. M. W. Kroesen and F. J. de Hoog, Journal of Applied Physics **70** (6), 2939 (1991).

[16] D. Hayashi, M. Nakamoto, N. Takada, K. Sasaki and K. Kadota, Japanese Journal of Applied Physics **38**, 6084 (1999).

[17] A. Kono and Y. Ohya, Japanese Journal of Applied Physics **39**, 1365 (2000).

[18] M. Haverlag, A. Kono, D. Passchier, G. M. W. Kroesen, W. J. Goedheer and F. J. de Hoog, Journal of Applied Physics **70** (7), 3472 (1991).

[19] G. A. Hebner and I. C. Abraham, Journal of Applied Physics **90** (10), 4929 (2001).

[20] G. A. Hebner and P. A. Miller, Journal of Applied Physics **87** (11), 7660 (2000).

[21] G. I. Font, W. L. Morgan and G. Mennenga, Journal of Applied Physics **91** (6), 3530 (2002).

[22] P. Ho, J. E. Johannes, R. J. Buss and E. Meeks, Journal of Vacuum Science & Technology A: Vacuum, Surfaces, and Films **19** (5), 2344 (2001).
[23] M. J. Kushner, Journal of Physics D: Applied Physics **42**, 194013 (2009).
[24] Y. Yang and M. J. Kushner, Plasma Sources Science and Technology **19** (5), 055011 (2010).
[25] Y. Yang, M. Strobel, S. Kirk and M. J. Kushner, Plasma Processes and Polymers **7**, 123 (2010).
[26] A. Vasenkov and M. Kushner, Physical Review E **66** (6), 066411 (2002).
[27] A. V. Vasenkov and M. J. Kushner, Journal of Applied Physics **94** (4), 2223 (2003).
[28] A. V. Vasenkov, X. Li, G. S. Oehrlein and M. J. Kushner, Journal of Vacuum Science & Technology A: Vacuum, Surfaces, and Films **22** (3), 511 (2004).
[29] M. Wang and M. J. Kushner, Journal of Vacuum Science & Technology A: Vacuum, Surfaces, and Films **29** (5), 051306 (2011).
[30] S.-X. Zhao, F. Gao, Y.-N. Wang and A. Bogaerts, Plasma Sources Science and Technology **21** (2), 025008 (2012).
[31] S.-X. Zhao, F. Gao, Y.-N. Wang and A. Bogaerts, Plasma Sources Science and Technology **22** (1), 015017 (2013).
[32] S.-X. Zhao, Y. R. Zhang, F. Gao, Y.-N. Wang and A. Bogaerts, J. Appl. Phys., **117**(24), 243303 (2015).
[33] G. A. Hebner, Journal of Applied Physics **89** (2), 900 (2001).
[34] X. Li, L. Ling, X. Hua, M. Fukasawa, G. S. Oehrlein, M. Barela and H. M. Anderson, Journal of Vacuum Science Technology A **21** (1), 284-293 (2003).
[35] H. H. Doh, J. H. Kim, K. W. Whang and S. H. Lee, J. Vac. Sci. Technol. A, **14**(3), 1088 (1996).
[36] M. Nagai and M. Hori, Journal of Vacuum Science & Technology A: Vacuum, Surfaces, and Films **24** (5), 1760 (2006).
[37] R. L. Woodin, M. S. Foster and J. L. Beauchamp, The Journal of Chemical Physics **72** (7), 4223 (1980).
[38] M. Sekine, Pure and Applied Chemistry **74** (3) (2002).
[39] M. Sekine, Applied Surface Science **192** (2002).
[40] F. Gaboriau, G. Cartry, M. C. Peignon and C. Cardinaud, Journal of Physics D: Applied Physics **39** (9) (2006).
[41] L. G. Christophorou, J. K. Olthoff and M. V. V. S. Rao, Journal of Physical and Chemical Reference Data **25** (5), 1341 (1996).
[42] G. A. Curley, D. Marić, J. P. Booth, C. S. Corr, P. Chabert and J. Guillon, Plasma Sources Science and Technology **16**, S87 (2007).
[43] H. K. Versteeg and Malalasekera, 2007 *An Introduction to Computational Fluid Dynamics: the Finite Volume Method* (England: Pearson Education Limited)
[44] D. A. Anderson, J. C. Tannehill, and R. H. Pletcher, 1984 *Computational Fluid Mechanics and heat transfer* (New York: McGraw-Hill, Inc)
[45] W. Liu, D. Q. Wen, S. X. Zhao *et al*, Plasma Sources Sci. Technol., **24**, 025035 (2015)
[46] J. T. Gudmundsson, J. Phys. D: Appl. Phys., **37**, 2073 (2004)